Structure-Function Dynamics of Engineered, Modular Neuronal Networks with Controllable Afferent-Efferent Connectivity

Nicolai Winter-Hjelm[1,✉], **Åste Brune Tomren**[2], **Pawel Sikorski**[2], **Axel Sandvig**[1,3,4,5], **and Ioanna Sandvig**[1]

[1]Department of Neuromedicine and Movement Science, Faculty of Medicine and Health Sciences, Norwegian University of Science and Technology (NTNU), Norway
[2]Department of Physics, Faculty of Natural Sciences, Norwegian University of Science and Technology (NTNU), Trondheim, Norway
[3]Department of Neurology and Clinical Neurophysiology, St Olav´s University Hospital, Trondheim, Norway
[4]Department of Clinical Neurosciences, Division of Neuro, Head and Neck, Umeå University Hospital, Umeå, Sweden
[5]Department of Community Medicine and Rehabilitation, Umeå University Hospital, Umeå, Sweden

Microfluidic devices interfaced with microelectrode arrays have in recent years emerged as powerful platforms for studying and manipulating *in vitro* neuronal networks at the micro- and mesoscale. By segregating neuronal populations using microchannels only permissible to axons, neuronal networks can be designed to mimic the highly organized and modular topology of neuronal assemblies in the brain. *In vivo*, the development of such neuronal assemblies is tightly orchestrated by reciprocal, dynamic structure-function relationships shaped by an interplay between intrinsic neuronal self-organizing properties and spatiotemporally regulated chemical and physical guidance cues. Engineered neuronal networks represent reductionist paradigms that can help recapitulate such dynamics *in vitro*. However, little is known about how the underlying topological features of such engineered neuronal networks contribute to their functional profile. To start addressing this question, a key parameter is control of afferent or efferent connectivity within the engineered network. In this study, we show that a microfluidic device featuring axon guiding channels with geometrical constraints inspired by a Tesla valve effectively promotes unidirectional axonal outgrowth between neuronal nodes, thereby enabling us to control afferent connectivity. We verified this by applying designer viruses to fluorescently label the neurons to visualise the structure of the networks, combined with extracellular electrophysiological recordings using embedded nanoporous microelectrodes to study the functional dynamics of these networks during maturation. We furthermore show that electrical stimulations of the networks induce signals selectively transmitted in a feedforward fashion between the neuronal populations. This model system has the potential to provide novel insights into the development, topological organization, and neuroplasticity mechanisms of neuronal assemblies at the micro- and mesoscale in healthy and perturbed conditions.

Self-organization | Signal propagation | Axon growth | Axonal pathfinding | Electrophysiology | Microdevice

Correspondence: ***nicolai.winter-hjelm@ntnu.no***

Introduction

Since the pioneering work by Taylor *et al.* in 2003, advancements in microfluidic technologies have been widely adapted by the neuroscience community for preclinical neuroscience research(1). The ability to segregate and integrate neuronal populations across compartmentalized microfluidic chips has facilitated construction of more robust, physiologically relevant model systems for studying neuronal networks *in vitro* with unparalleled experimental control. However, these platforms do not inherently aid establishment of feedforward projection sequences. Such a topological organization is critical for promoting directional and hierarchical information processing, as can be seen in a range of brain areas, such as the laminar structure of the neocortex, the cerebrocerebellar loop and the entorhinal-hippocampal loop, to mention a few(2). *In vivo*, a complex interplay between mechanical and chemical guidance cues steers the establishment of such structural and functional connections(3–5). *In vitro*, dissociated neurons are seeded in a rather homogeneous environment lacking mechanical or chemical gradients to direct the establishment of directional projection sequences. While neuroengineering approaches have advanced significantly over the past two decades, there consequently still remains a need for more sophisticated model systems that can efficiently promote directional axonal outgrowth and establishment of controllable afferent-efferent structural and functional connections.

Intrinsic axonal growth and guidance programs combined with cues from the microenvironment enable the growth cone at the tip of axons and their collaterals to probe their environment as part of axonal pathfinding(3, 5). Over the past decade, a growing body of literature has demonstrated the effectiveness of microfluidic devices with geometrical constraints implemented within the microchannel architecture to steer the directionality of axonal outgrowth *in vitro*(6–13). This is used to promote axonal outgrowth in a single direction, while outgrowth in the opposite direction is impeded(14). Effectively, such topological constraints supports the establishment of predefined pre- and postsynaptic populations of neurons, where the presynaptic population projects connections to the postsynaptic population, but not the other way around. The first documented attempt at promoting unidirectional axon growth in this way was made by Peyrin *et al.* in 2011, demonstrating that a design with narrower inlets at the postsynaptic side effectively reduced the chance of axons growing into the microchannels so that mainly axons from the presynaptic populations filled up the channels(6). Others have used variations of bottlenecks and traps inside the channels to coax the axons from the postsynaptic population away from the main channels and make them retract(7–10).

More recent studies have steered the afferent-efferent connectivity by implementing topographical features within the microchannels that guide the neurites from the presynaptic population through the channels, while the axons from the postsynaptic population are guided away from the main channels and back to their chamber of origin(11–13). An advantage with the latter approach is that it circumvents axonal

degeneration within the channels, which otherwise can give rise to harmful debris that hinders the axons from the presynaptic population and confounds imaging. Studies in which the neuronal populations have been seeded at different time points have also been shown efficient at promoting unidirectional connectivity within microdevices(15). However, this approach causes the neuronal populations to be at different maturation stages throughout the experimental period, and becomes particularly impractical when creating more complex systems with more than two neuronal populations. For this reason, a combination of topographical structures that effectively promote pathfinding into the channels from the presynaptic population, retard the axons from the postsynaptic neurons from finding the inlets to the channels, and also redirect the axons from the postsynaptic population that manage to enter the channels back to their chamber of origin have the potential to effectively promote unidirectional axonal growth(13).

To improve the robustness of engineered neuronal networks *in vitro* as models of neuronal networks in the brain, the duration of the experiments is also of major importance. While all previously cited studies reported adequate control of unidirectional connectivity, they were limited to short periods of time, and at most three weeks from culture initiation. Even at this point, most neuronal networks are still immature and will undergo continued axonal outgrowth, fasciculation, and eventually synaptic pruning before the networks reach maturity and have formed stable structural and functional connections. Furthermore, the way in which topographical features and modular organization affect the functional connectivity and signal propagation within engineered neuronal networks is still largely underexplored. As such, there is a need for experimental platforms which reliably and longitudinally support the study of dynamic structure-function relationships in engineered *in vitro* neuronal networks during prolonged periods of times.

In this study, we use geometrical constraints inspired by the Tesla valve design to control afferent-efferent connectivity of rat cortical neurons. The Tesla valve was originally designed by Nikola Tesla more than 100 years ago to allow fluids to preferentially flow in a single direction without the assistance of any moving mechanical parts(16). The geometry of the design promotes liquid flow in the forward direction, while the liquid is looped back on itself when moving in the backward direction to effectively create an impenetrable barrier. Used in combination with the phenomena of laminar flow found in microfluidics, this valvular conduit has as such proven highly efficient at controlling liquid flows(17). Here, we show that the same design can be used to consistently establish neuronal networks with definable connectivity, and we furthermore demonstrate a powerful method for both evaluating the structure and function of these networks longitudinally up to four weeks or longer *in vitro*. This opens up an avenue for establishing more robust reductionist paradigms of *in vivo* neuronal networks to recapitulate and study the development and function of the complex topological structures of the brain in both health and disease. Additionally, our design promotes highly efficient liquid separation between the neuronal populations which can be useful in a range of applications, such as disease modelling and drug screening.

Experimental

Design of Experimental Platform. Designs for the microdevices were created using the CAD software Clewin 4 (WieWeb Software, Enschede), and are illustrated in **Figure S2**. The microfluidic platforms comprised two $5\,\mathrm{mm}$ wide and $60\,\mu\mathrm{m}$ high compartments, henceforth referred to as nodes, connected by 20 microchannels, each $700\,\mu\mathrm{m}$ long, $10\,\mu\mathrm{m}$ wide and $5\,\mu\mathrm{m}$ high. The compartments employed a partially open design, initially demonstrated by van de Wijdeven *et al.*(18), to aid high experimental control and reproducibility. To promote unidirectional axonal growth, geometrical constraints inspired by the Tesla valve design were incorporated in the microfluidic channels to redirect axons from the postsynaptic side to the chamber from which they originated. Furthermore, axon traps were incorporated on the postsynaptic side to misguide any outgrowing axons, inspired by the work of Renault *et al.*(13) A pattern of $4\,\mu\mathrm{m}$ diameter pillars with $4\,\mu\mathrm{m}$ interspacing was positioned on the presynaptic side to prevent neuronal somata from entering and blocking the channels. For the two-nodal microfluidic devices interfaced with microelectrode arrays (n = 5), 59 electrodes of $50\,\mu\mathrm{m}$ diameter were positioned evenly spread across the chips, of which 10 electrodes were placed selectively in the channels to confirm active connections between the neuronal populations. A reference electrode was split between the two chambers. Platforms with a single chamber interfaced with microelectrode arrays were used as controls (n = 6), in which the total seeding area was equal to the two-nodal devices. An experimental timeline is shown in **Figure 1**.

Fabrication of Microfluidic MEAs.

Mould for Microfluidic Chips . A soft lithography mould was made by application of a photoresist pattern on a 4-inch silicon wafer (Siltronix). The wafer was washed consecutively in acetone and isopropanol (IPA) for $1\,\mathrm{min}$ each to remove organic contaminants, followed by a plasma clean for $5\,\mathrm{min}$ in $100\,\mathrm{sccm}$ O_2 plasma at $20\,\mathrm{kHz}$ generator frequency (Femto Plasma Cleaner, Diener Electronics). A $5\,\mathrm{min}$ dehydration bake was conducted at $150\,^{\circ}\mathrm{C}$ to remove moisture. The photoresist mr-DWL5 (micro resist Technology GmbH) was spin coated onto the substrate in two steps of $3000\,\mathrm{rpm}$ for $35\,\mathrm{s}$ at $1000\,\mathrm{rpm/min}$ and $4000\,\mathrm{rpm}$ for $2\,\mathrm{s}$ at $2000\,\mathrm{rpm/min}$, respectively, to achieve a final thickness of $5.0\,\mu\mathrm{m}$ (spin150, SPS-Europe B.V.). A soft bake was subsequently conducted, starting at $50\,^{\circ}\mathrm{C}$ for $2\,\mathrm{min}$ before gradually increasing the temperature to $90\,^{\circ}\mathrm{C}$ ($10\,^{\circ}\mathrm{C\,min^{-1}}$) where it was kept for $2\,\mathrm{min}$. The wafer was left to cool down on the hotplate ($10\,^{\circ}\mathrm{C\,min^{-1}}$), before being left at room temperature (RT) to rest for $10\,\mathrm{min}$. A maskless aligner (MLA150, Heidelberg) was used to transfer the MEA design onto the resist with a $405\,\mathrm{nm}$ laser at $300\,\mathrm{MJ/cm^2}$. After ex-

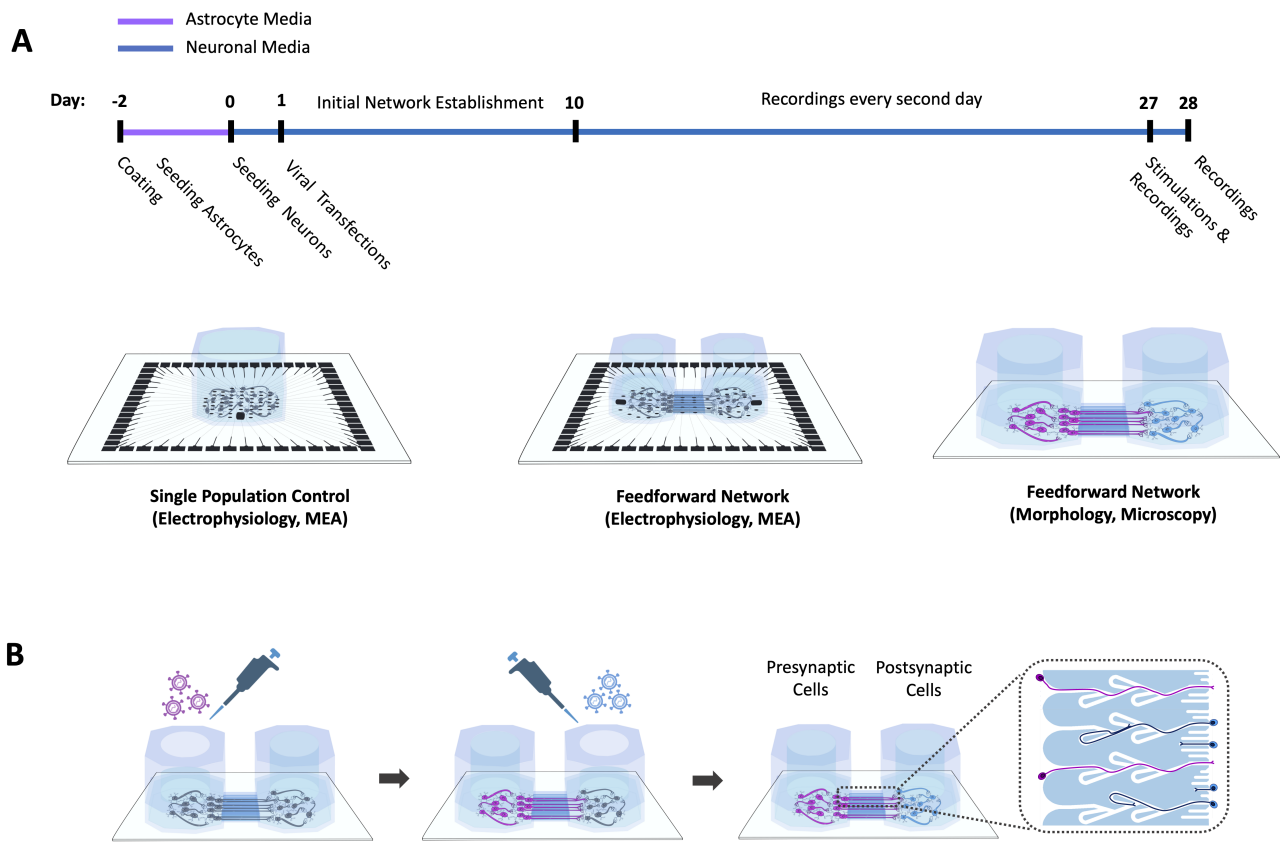

Figure 1 | Experimental timeline. **(A.)** Neurons were grown in microdevices either interfaced with glass coverslips or MEAs. The neurons grown in microfluidic devices interfaced with microelectrode arrays were recorded every second day from 10 DIV to 28 DIV and stimulated at 27 DIV. **(B.)** Neurons grown in microfluidic chips interfaced with glass coverslips were transfected with AAV 2/1 with a CMV promoter to induce ubiquitous expression of different fluorescent proteins in the two cell populations on DIV 1. This facilitated examination of the presence of axons from the pre- and postsynaptic populations within the microchannels throughout network development. The schematics are not to scale.

posure, the film was post exposure baked equivalently to the soft bake, before being left to rest at RT for 1 h. The film was subsequently developed in mr-Dev 600 (micro resist Technology GmbH) for 120 ± 15 s before thoroughly rinsed in IPA. The substrate was thereafter hard baked at 120 °C for 30 min.

A second layer of photoresist mr-DWL40 (micro resist Technology GmbH) was spin coated onto the substrate in two steps of 1200 rpm for 30 s at 500 rpm/min and 3500 rpm for 5 s at 1000 rpm/min, respectively, to achieve a final thickness of 60 µm. A soft bake was consecutively conducted, starting at 50 °C for 5 min before gradually increasing the temperature to 90 °C (10 °C min^{-1}) where it was kept for 10 min. The wafer was left to cool down on the hotplate (10 °C min^{-1}), before being left to rest at RT for 1 h. The film was exposed with a 405 nm laser at 600 $\mathrm{MJ/cm^2}$. After exposure, the film was post exposure baked equivalently to the soft bake, before being left to rest at RT overnight. The film was subsequently developed in mr-Dev 600 (micro resist Technology GmbH) for 300 ± 15 s before thoroughly rinsed in IPA. The substrate was hard baked at 120 °C for 30 min. A profilometer (Dektak 150, Veeco) was used to confirm the intended heights. The finalized mould was eventually silanized (trichloro(1H,1H,2H,2H-perfluorooctyl(97 %)), Sigma-Aldrich) in vacuum for 2 h.

Microfluidic Chips . Silicon elastomer and curing agent (SYLGARD®184 elastomer kit, Dow Corning) was mixed, degassed, and cast in the photoresist mould at a ratio of 10:1. The PDMS was cured in an oven (TS8056, Termaks) at 65 °C for 4 h. The PDMS was peeled from the mould, and cell compartments were cut out with a 4 mm diameter puncher. PDMS debris was removed using scotch tape, and the chips subsequently washed in acetone, 96 % ethanol and DI water for 1 min each. The chips were eventually left to dry overnight.

Microelectrode Arrays . The protocols for fabrication of microelectrode arrays were adapted and partly modified from van de Wijdeven *et al.*(19). 1 mm thick 4-inch borosilicate wafers (100 mm Borofloat33, Plan Optik) were used as substrates for the MEAs. The wafers were washed subsequently in acetone and IPA for 1 min each to remove organic contaminants, before being plasma cleaned for 5 min in 100 sccm O_2 plasma at 20 kHz generator frequency. A 2 min dehydration bake was conducted at 100 °C to remove moisture. The photoresist ma-N 440 (micro resist Technology GmbH)

was spin coated onto the substrates at $3000\,\mathrm{rpm}$ for $42\,\mathrm{s}$ at $500\,\mathrm{rpm/min}$ for a final thickness of $4\,\mu\mathrm{m}$ (spin150, SPS-Europe B.V.). The film was left to rest for $10\,\mathrm{min}$ before being soft baked at $95\,°\mathrm{C}$ for $5\,\mathrm{min}$. A maskless aligner (MLA150, Heidelberg) was used to transfer the MEA design onto the resist with a $405\,\mathrm{nm}$ laser at $1800\,\mathrm{MJ/cm^2}$. After exposure, the resist was developed in ma-D332/s (micro resist Technology GmbH) for $90 \pm 10\,\mathrm{s}$ before thoroughly rinsed in DI water. Prior to e-beam evaporation, the substrates were descummed in $100\,\mathrm{sccm}$ O_2 plasma for $1\,\mathrm{min}$ at $20\,\mathrm{kHz}$ generator frequency. An adhesive layer of $50\,\mathrm{nm}$ titanium was evaporated onto the substrates at $5\,\mathrm{Å\,s^{-1}}$, followed by $100\,\mathrm{nm}$ platinum at $2\,\mathrm{Å\,s^{-1}}$ (E-beam Evaporator, Pfeiffer Vacuum Classic 500). A lift-off process was subsequently conducted in acetone before the wafers were rinsed in IPA.

Prior to passivation layer deposition, another descum was conducted for $1\,\mathrm{min}$. Next, a $470\,\mathrm{nm}$ thick insulation layer of silicon nitride (Si_3N_4) was deposited on the substrates using plasma enhanced chemical vapour deposition at $300\,°\mathrm{C}$ for $30\,\mathrm{min}$ consisting of $20.0\,\mathrm{sccm}$ SiH_4, $20.0\,\mathrm{sccm}$ NH_3 and $980\,\mathrm{sccm}$ N_2 gas (PlasmaLab System 100-PECVD, Oxford Instruments). A second lithographic step was conducted using ma-N 440 according to the same protocol as previously described to define an etch mask. Inductively coupled plasma with $50.0\,\mathrm{sccm}$ CHF_3, $10.0\,\mathrm{sccm}$ CF_4 and $7.0\,\mathrm{sccm}$ O_2 gas for $6.5\,\mathrm{min}$ was subsequently used to dry etch the silicon nitride above the electrodes and contact pads (Plasmalab System 100 ICP-RIE 180, Oxford Instruments).

A thin layer of platinum black was eventually electrodeposited on the electrodes (PP-Type Wafer Plating Electroplating Laboratory System, Yamamoto). The electrolyte bath consisted of aqueous $2.5\,\mathrm{mmol}$ chloroplatinic acid (H_2PtCl_6, $8\,\mathrm{wt\%}$ H_2O, Sigma-Aldrich, 262587), in which the wafers were partially submerged using a custom-built wafer holder so that the liquid only covered the electrodes and not the contact pads (illustrated in **Figure S1B**). A Red Rod REF201 Ag/AgCl electrode (Hatch) was used as reference, and a platinized titanium plate as counter electrode. A paddle agitator was used at $60.0\,\mathrm{rpm}$ to reduce diffusion thickness, and the temperature was kept constant at $30\,°\mathrm{C}$ by an external temperature controller. A Palmsens 4 potentiostat (Palmsens) was used in chronoamperometric mode with a constant voltage of $-0.4\,\mathrm{V}$ for $3\,\mathrm{min}$ for all depositions. Eventually, the substrates were diced into 48x48 mm square MEAs with a wafer saw (DAD323, DISCO). The photoresist masks were subsequently stripped off in acetone, followed by a rinse in $96\,\%$ ethanol and DI water. To remove hardened photoresist and oxidize the top few nanometres of the silicon nitride layer into silicon dioxide (SiO_2), the surface was plasma cleaned for $10\,\mathrm{min}$ in $160\,\mathrm{sccm}$ O_2 at $32\,\mathrm{kHz}$ generator frequency.

Assembly of Microfluidic MEA Platforms . The microfluidic chips were bonded irreversibly to either MEAs or precleaned (acetone, $96\,\%$ ethanol and DI water) glass coverslips (24x24 mm Menzel-Gläser, VWR International). Both microfluidic chips and MEAs/coverslips were plasma cleaned with O_2 plasma for $1\,\mathrm{min}$ in $200\,\mathrm{sccm}$ O_2 plasma at $40\,\mathrm{kHz}$ generator frequency. Directly after, the PDMS chips were pushed gently onto the MEAs/coverslips. To facilitate alignment of the microfluidic chips to the MEAs, two drops of $70\,\%$ ethanol were placed in between the PDMS chip and the MEA, and alignment was performed under a stereomicroscope (Nikon SMZ800). For both coverslips and MEAs, bonding was finalized on a hotplate at $100\,°\mathrm{C}$ for $1\,\mathrm{min}$ followed by $5\,\mathrm{min}$ at RT under gentle pressure. To remove traces of ethanol from the platforms, three subsequent washes in DI water were conducted with $10\,\mathrm{min}$ intervals. Finally, the chips were filled with DI water to maintain hydrophilicity and sterilized in UV light overnight in a biosafety cabinet.

Cell Culturing and Staining.

Coating of Culturing Platforms. After sterilization, DI water was replaced by $0.1\,\mathrm{mg/ml}$ Poly-L-Ornithine solution (PLO) (Sigma-Aldrich, A-004-C) and the chips incubated at $37\,°\mathrm{C}$ and $5\,\%$ CO_2 for $30\,\mathrm{min}$. Subsequently, the PLO was replaced by fresh PLO, and the chips incubated at $37\,°\mathrm{C}$ and $5\,\%$ CO_2 for another hour. Next, the chambers were washed three times with MQ water, before being filled up with laminin solution consisting of Leibovitz-15 Medium (Sigma-Aldrich, L5520) supplemented with $45.6\,\mathrm{mg/ml}$ sodium bicarbonate (Sigma-Aldrich, S6014) and $16\,\mu\mathrm{g/ml}$ natural mouse laminin (Gibco™, 23017015) and incubated at $37\,°\mathrm{C}$, $5\,\%$ CO_2 for $30\,\mathrm{min}$. Subsequently, the laminin solution was replaced with fresh laminin solution, and the chips incubated for another $2\,\mathrm{h}$. During all coating steps, a hydrostatic pressure gradient was created between the chambers by filling one chamber fuller than the other to assure proper flow of coating solution through the microfluidic channels.

Cell Seeding and Maintenance. Laminin solution was replaced by astrocyte media consisting of DMEM, low glucose (Gibco™, 11885084) supplemented with $15\,\%$ Fetal Bovine Serum (Sigma-Aldrich, F9665) and $2\,\%$ Penicillin-Streptomycin (Sigma-Aldrich, P4333). Rat astrocytes (Gibco™, N7745100) were consecutively seeded at a density of $100\,\mathrm{cells/mm^2}$, i.e., 2000 cells per microchamber in the two compartmental devices and 4000 cells in the single compartmental devices. After two days of expansion, the astrocyte media was replaced with neuronal media consisting of Neurobasal Plus Medium (Gibco™, A3582801) supplemented with $2\,\%$ B27 Plus (Gibco™, A358201), $1\,\%$ GlutaMax (Gibco™, 35050038) and $2\,\%$ Penicillin-Streptomycin (Sigma-Aldrich, P4333). Additionally, Rock Inhibitor (Y-27632 dihydrochloride, Y0503, Sigma-Aldrich) was added at a concentration of $0.1\,\%$ during seeding to increase survival rate. Pen-strep was not included in the microfluidic chips used for viral transfections until 4 DIV to avoid potential interference with transfection efficacy. Rat cortical neurons from Sprague Dawley rats (Gibco, A36511) were seeded at a density of $1000\,\mathrm{cells/mm^2}$, equalling 20 000 cells per well in the two-nodal platforms and 40 000 cells in the controls. Half the cell media was replaced with fresh cell media 4 hours after seeding, and again after $24\,\mathrm{h}$. From here on, half the cell media was replaced every second day until the cultures were

ended at 28 DIV.

Viral Transfections. To assess the efficacy of the device at promoting unidirectional axonal growth, neurons in two-compartmental devices on glass coverslips were virally transfected with an AAV 2/1 serotype loaded with either pAAV-CMV-beta Globin intron-EGFP-WPRE-PolyA or pAAV-CMV-beta Globin intron-mCherry-WPRE-PolyA. This was done to make the two cell populations ubiquitously express different fluorescent proteins, aiding longitudinal monitoring of the structural connectivity in the microchannels during development. Transfections were started one day after seeding. A hydrostatic pressure gradient was used during the transfection to hinder viral leakage between the two nodes. 3/4 of the media in the presynaptic chamber was removed, and AAV 2/1 viruses with a CMV promoter encoding GFP were added at a titer of approximately $5e^2$ viruses/cell ($1e^7$ viruses per chamber). The cells were incubated at $37\,°\mathrm{C}$ and $5\,\%$ CO_2 for $3\,\mathrm{h}$. Next, the presynaptic well was filled up with fresh neuronal media, and 3/4 of the media in the postsynaptic chamber were removed. AAV 2/1 viruses with a CMV promoter encoding mCherry was furthermore added to the postsynaptic chamber at a titer of $5e^2$ viruses/cell. The postsynaptic well was subsequently filled all the way up again after $3\,\mathrm{h}$. Viral vectors were prepared in-house at the Viral Vector Core Facility, NTNU.

Images were acquired using an EVOS M5000 microscope (Invitrogen) using DAPI (AMEP4650), CY5 (AMEP4656), GFP (AMEP4651) and TxRed (AMEP4655) LED light cubes and Olympus UPLSAP0 4X/0.16 NA and 20x/0.75 NA lenses. Post-processing of images was conducted in ImageJ with the Fiji plugin to change the selected colour channels and add scale bars.

Immunocytochemistry. For immunocytochemistry, cells were seeded in µ-slide 8 Wells (Ibidi, GmbH, 80826) following the same protocol as for the microfluidics. Fixation was done using glyoxal solution based on the protocol by Richter *et al.*(20). The solution consisted of $71\,\%$ MQ water, $20\,\%$ ethanol absolute (Kemetyl, $100\,\%$), $7.8\,\%$ Glyoxal solution (Sigma-Aldrich, 128465) and $1\,\%$ acetic acid (Sigma-Aldrich, 1.00063). Cell media was replaced with the fixative and incubated at RT for $15\,\mathrm{min}$, before washing the chambers with phosphate-buffered saline (PBS, Sigma-Aldrich, D8537) 3 times for $5\,\mathrm{min}$ each. Permeabilization was conducted using $0.5\,\%$ Triton-X (Sigma-Aldrich, 1086431000) diluted in PBS for $5\,\mathrm{min}$, before the wells were washed 2 consecutive times in PBS for $5\,\mathrm{min}$. Next, blocking solution consisting of $5\,\%$ goat serum (Abcam, ab7481) diluted in PBS was added to the wells, and the chips were left to incubate at RT on a shaking table at $30\,\mathrm{rpm}$ for $1\,\mathrm{h}$. The blocking solution was thereafter replaced by primary antibodies mixed with $5\,\%$ goat serum in PBS. A full overview of primary antibodies and their respective concentrations are listed in Table 1. The chips were subsequently placed on a shaker table at $30\,\mathrm{rpm}$ at $4\,°\mathrm{C}$ overnight. The following day, secondary antibody solution was prepared consisting of $0.2\,\%$ secondaries and $5\,\%$ goat serum diluted in PBS. Prior to mixing, the secondary antibodies were centrifuged at $6000\,\mathrm{rpm}$ for $15\,\mathrm{min}$ to remove precipitates. Next, the primary antibody solution was removed from the wells, and the wells washed three times with PBS for $5\,\mathrm{min}$. Subsequently, secondary antibody solution was added to the wells, and the cells incubated at RT on a shaker table at $30\,\mathrm{rpm}$ for $3\,\mathrm{min}$ in the dark. After this, the secondary antibody solution was replaced by solution consisting of the nuclear stain Hoechst (Abcam, ab228550) at a concentration of 1/2000 diluted in PBS and incubated at a shaking table at RT for $30\,\mathrm{min}$. Finally, the chips were once again washed three times in PBS for $5\,\mathrm{min}$ each, then once in MQ water for $5\,\mathrm{min}$, before eventually being filled halfway up with MQ water for imaging.

Table 1 Antibodies and concentrations used for Immunocytochemistry

Marker	Catalogue Number	Concentration
$\beta 3 - Tubulin$	Ab78078	1/1000
Doublecortin	Ab153668	1/200
GABA	Ab86186	1/1000
GFAP	Ab7260	1/1000
MAP2	Ab5382	1/5000
NeuN	Ab279295	1/500
Neurofilament Heavy	Ab4680	1/5000
PSD95	Ab13552	1/250
Synaptophysin	Ab32127	1/500
Tbr1	Ab183032	1/100

All antibodies were purchased from Abcam.

Imaging was conducted using a Zeiss 800 Airyscan Confocal Laser Scanning Microscope (CLSM) with Zeiss Zen Blue software. The microscope was equipped with a LSM 800 Laser Module URGB with diode lasers $405\,\mathrm{nm}$ ($5\,\mathrm{mW}$), $488\,\mathrm{nm}$ ($10\,\mathrm{mW}$), $561\,\mathrm{nm}$ ($10\,\mathrm{mW}$) and $640\,\mathrm{nm}$ ($5\,\mathrm{mW}$). A Zeiss Axiocam 503 color camera, 2.8 Mpix, 38 fps (color) was furthermore used for image acquisition.

Sample Dehydration and SEM Imaging. For the full protocol, see supplementary materials.

Electrophysiology and Data Analysis.

Electrophysiological Recordings. The average impedance of the electrodes was measured to $34.5 \pm 10.9\,\mathrm{k\Omega}$ in $0.1\,\%$ PBS Solution using an MEA-IT60 System (Multichannel Systems). Recordings were conducted using a MEA2100 workstation (Multichannel Systems) at a sampling rate of $25\,000\,\mathrm{Hz}$. A temperature controller was used to maintain temperature at $37\,°\mathrm{C}$ (TC01, Multichannel Systems). A 3D-printed plastic construct covered by a gas-permeable membrane was used to keep the cultures sterile during recordings. Prior to recordings, the networks were allowed to equilibrate for $5\,\mathrm{min}$ at the recording stage. Each recording lasted for $15\,\mathrm{min}$, and recordings were always conducted on the day following media changes.

Electrical stimulations. Stimulations were performed at 27 DIV using a train of 60 spikes at $\pm\,800\,\mathrm{mV}$ (positive phase first) of $200\,\mu\mathrm{s}$ duration with an inter spike interval of $5\,\mathrm{ms}$.

Prior to stimulation, a baseline recording of 5 min was conducted to identify the most active electrode close to the centre of the chamber measured in number of spikes/s, which was subsequently chosen for stimulation. For the two-nodal platforms, the most active electrode in the postsynaptic node was stimulated first, followed by the most active electrode in the presynaptic node.

Data Analysis. All data analysis, including filtering and spike detection, was conducted in Matlab R2021b using a combination of borrowed and custom-made scripts. Raw data was filtered using a 4th order Butterworth bandpass filter, removing high frequency noise (above 3000 Hz) and low frequency fluctuations (below 300 Hz). A notch filter was used to remove 50 Hz noise caused by the mains hum. Both filters were run using zero-phase digital filtering using the Matlab function filtfilt to avoid changes in the relative position of the detected spikes. Spike detection was conducted using the Precise Timing Spike Detection (PTSD) algorithm developed by Maccione *et al.*(21) The threshold was set to 11 times the standard deviation of the noise, the maximum peak duration to 1 ms and the refractory time to 1.6 ms.
Burst detection was subsequently performed using the logISI approach developed by Pasquale *et al.*(22), with a minimum of 4 consecutive spikes set as a threshold for a burst to be detected. The hard threshold for the interspike interval both within and outside of the burst core was set to 100 ms. These numbers were chosen based on the original manuscript reporting the method(22), as well as manual inspection of the burst detection performance. For analysis of spontaneous network activity, network bursts were furthermore detected using the logIBEI approach(23), with at least 20 % of all active electrodes in the network required to participate for the activity to be classified as a network burst. Network synchrony was measured using the coherence index, as described by Wang(24).
For each network burst, the spiking activity of each node was binned into 20 ms bins, and the resulting tuning curves of the two nodes plotted. If a network burst was detected, but only one of the nodes had more than 30 detected spikes within the time span of the network burst, the network burst was evaluated as contained within that individual node. If more than 30 spikes were detected within both nodes, the network burst was considered to have propagated between the nodes. If the network burst was found to spread between the two nodes, the temporal position of the peaks of the two tuning curves were compared to evaluate whether the network burst spread from the pre- to the postsynaptic node or vice versa. Only response delays between 40 ms to 200 ms were included in the analysis as delays shorter or longer than this made it difficult to infer directionality or made it unlikely for the activity to be part of the same network burst, respectively. This delay time is also consistent with the delay times reported by others(25).
Stimulation data was run through the SALPA filter developed by Wagenaar *et al.*(26), and each stimulated time point was followed by 15 ms blanking to avoid stimulation artifacts being detected as spikes. Peristimulus time histograms were made for each platform by binning the data in the 300 ms following a stimulation into 20 ms time bins, and the average response of the network in each bin for the 60 individual stimulations was plotted. Raster plots were made using a customized version of the SpikeRasterPlot function developed by Kraus(27). Heatmaps showing 20 ms binned network activity following stimulations were created using a customized version of the Matlab function heatmap developed by Deoras(28).
Spike data for the spontaneously evoked activity was binned into 50 ms time bins, and functional connectivity was evaluated using pairwise mutual information throught the information theory toolbox developed by Timme & Lapish(29). Graph theoretical metrics were calculated using the Brain Connectivity Toolbox developed by Rubinov & Sporns(30). These were furthermore used to plot custom designed graphs showing node colour as spike frequency (spikes/s), node size as PageRank centrality, edge colour as the functional connectivity (pairwise mutual information) and node edge colour as the community calculated using the Louvain algorithm. Nodes were positioned according to the relative position of the electrodes on the actual microfluidic MEAs. Average graph metrics were also plotted over time.
For all plots, customized colormaps were created using the Matlab versions linspecer(31) and colorBrewer2(32), based on the web tool colorBrewer developed by Brewer *et al.*(33).

Results & Discussion

Tesla Valve Inspired Design Promotes Unidirectional Connectivity Establishment Between Neuronal Nodes

In Vitro. Dissociated neurons were seeded on top of an astrocyte feeder layer in two-compartmental microfluidic chips separated by 5 µm high, 10 µm wide and 750 µm long microchannels only permissible to their axons. Designs inspired by the Tesla valve were implemented in the microchannel architecture to promote unidirectional connectivity between the two neuronal nodes. Expression of the fluorescent proteins from the viral transfections used to assess the structural connectivity was observed after 7 – 14 DIV. While the design is particularly suited for keeping the liquid content of the two compartments separated, some leakage of viruses between the chambers was observed (**Figure 2**). Yet, the number of neurons inadvertently transfected by viruses leaking from the opposite chamber was found to be consistently low. Repeated washings of the microchambers with neuronal media three hours after transfections were initiated reduced the leakage of viruses between the nodes, but at the same time gave more inconsistent transfection efficiencies across the chips. Therefore, the chambers were filled with media three hours after the addition of the viruses and the devices were left unperturbed for 48 hours.
We found that the efficiency of the microdevice design in facilitating asymmetric axon growth could be tuned by the dimensions of the Tesla loops. A loop diameter of 40 µm, height of 60 µm and channel turning angle of 140° was found to promote directionality with primarily axons from the presynaptic node filling up the microchannels. Yet, as the networks matured and the channels filled up with axons

from the presynaptic node, axons from the postsynaptic node managed to grow in a zig-zag pattern within the Tesla loops to reach the opposite node (**Figure 2A**). As this was undesired, the loops were redesigned. Decreasing the loop diameter to 30 µm and increasing the height to 70 µm (**Figure 2B**) resulted in more efficient control of the afferent connectivity by directing the axons from the postsynaptic node back to the chamber of origin within the first few Tesla loops. Controls with bidirectional microchannels were also tested to demonstrate the bilateral growth of axons in the channels in the absence of any geometrical constraints (**Figure S4**).

To further assess the robustness of our approach, geometries based on previously published designs were fabricated and compared with the Tesla valve design when using the same cell culture conditions (**Figure S5**). Designs implementing trapping structures within the channels, similar to the one demonstrated by Gladkov *et al.*(9), were commonly found to cause extensive fragmentation of axons within the channels. This effectively caused accumulation of cell debris within the trapping structures, furthermore hindering axons from the presynaptic population from reaching the opposite node, as well as confounding imaging. Designs redirecting the axons, such as the loop-back design originally demonstrated by Renault *et al.*(13) were found to be more effective, but still allowed multiple axons from the postsynaptic node to reach the presynaptic node, as illustrated in **Figure S5A**.

Structural Maturation is Crucial for Afferent-Efferent Network Connectivity. Fixation and immunocytochemistry were performed after 7, 14 and 21 DIV to assess the development, maturation and connectivity of the neuronal cultures. Neurons were co-cultured with astrocytes and seeded in 8-well Ibidi chips, and the presence of mature cytoskeletal and synaptic markers, as well as both excitatory and inhibitory activity verified. A Zeiss 800 Airyscan Confocal Laser Scanning Microscope was used for imaging the cultures. Doublecortin and Growth-Associated Protein 43 (GAP43) have both been found critical for neurodevelopment and growth cone migration, respectively, and were used as markers for immature neurons. The cytoskeletal markers Microtubule-Associated Protein 2 (MAP2) and β3-Tubulin starts being expressed shortly after axonogenesis and continue to be expressed as the cells mature. These markers were used to assess structural network maturation, indicating aggregation of neuronal somata and dense fasciculation already after 14 DIV (**Figure 3A**). The expression of Neuronal Nuclear Protein (NeuN) and Neurofilament Heavy (NFH) were used as markers for mature neurons. Both markers were expressed at 21 DIV (**Figure 3B**). GFAP was used to stain for the astrocytic feeder layer in each network. Colocalization of synaptophysin and PSD95 were used to verify the presence of mature synaptic connections (**Figure 3C**). Furthermore, the presence of glutamate receptors and GABA were used to confirm presence of both excitatory and inhibitory activity in the network (**Figure 3D**). Images showing the development in expression profiles of the neuronal and astrocytic markers over time can be seen in the supplementary materials (**Figure S3**). As can be clearly delineated from these images, fluorescence intensity of NFH was significantly higher at 21 DIV compared to 14 DIV. There was also a high expression of GAP43 even at 21 DIV, indicating that the networks were still undergoing substantial axonal outgrowth, and thereby structural maturation at this point. This clearly underlines the need for monitoring of the structural connectivity of these networks beyond 21 DIV, which is the maximum observation window reported in the relevant literature, to assess the efficacy of various designs at promoting establishment of unidirectionally coupled neuronal circuitries.

Spontaneous Activity Spreads in a Feedforward Manner Following Connectivity Establishment Between the Two Nodes. To evaluate the effect of the controlled afferent connectivity on network activity, neuronal cultures were grown on microfluidic chips interfaced with customized microelectrode arrays to facilitate measurements of their electrophysiological activity (**Figures 4A** & **4B**). Given the high temporal resolution of spikes detected using MEA recordings, this approach was suitable both for assessing the functional connectivity within each node and for tracking signal propagation between them with high accuracy. To increase the signal-to-noise ratio of the noisy extracellular recordings in the open compartments, nanoporous platinum black was deposited on the MEA electrodes (**Figures 4C** & **4D**). Electrodes were also placed in the microchannels to verify connectivity between the nodes ((**Figures 4E** & **4F**)).

Spontaneous network bursts were detected and used to analyse the network activity. Individual bursts were characterised as events with a minimum of four consecutive spikes as identified using the logISI approach described in the methods section, and network bursts as events where at least 20 % of the active electrodes displayed bursting activity simultaneously. As individual spikes are challenging to track between the nodes, bursts were consequently used to evaluate whether signals primarily moved from the pre- to the postsynaptic node. As detailed in the methods section, tuning curves of both nodes were created and their peak identified to evaluate the temporal spread of synchronized activity between them. Resulting tuning curves of a network burst spreading from the pre- to the postsynaptic node, and vice versa, are shown in **Figure 5A**. For unidirectionally connected nodes, one would expect a majority of the signals to either propagate from the pre- to the postsynaptic node, or remain within the individual nodes, of which the latter would suggest lack of internodal functional connectivity. The number of network bursts contained within each node, or propagating in either direction between them, are shown in **Figure 5B**. Given the structural variability between the individual networks, the activity in each microdevice was analysed separately. At DIV 10-12, the individual nodes had started exhibiting network wide bursts. Bursts were initially found to establish independently and at a similar rate in both nodes in a single microdevice. At around three weeks *in vitro*, three out of five two-nodal unidirectionally connected networks appeared to have sufficient structural connectivity to enable transmission of network bursts from the pre- to the postsynaptic node. A minor fraction of the network bursts was analysed as spreading between the nodes

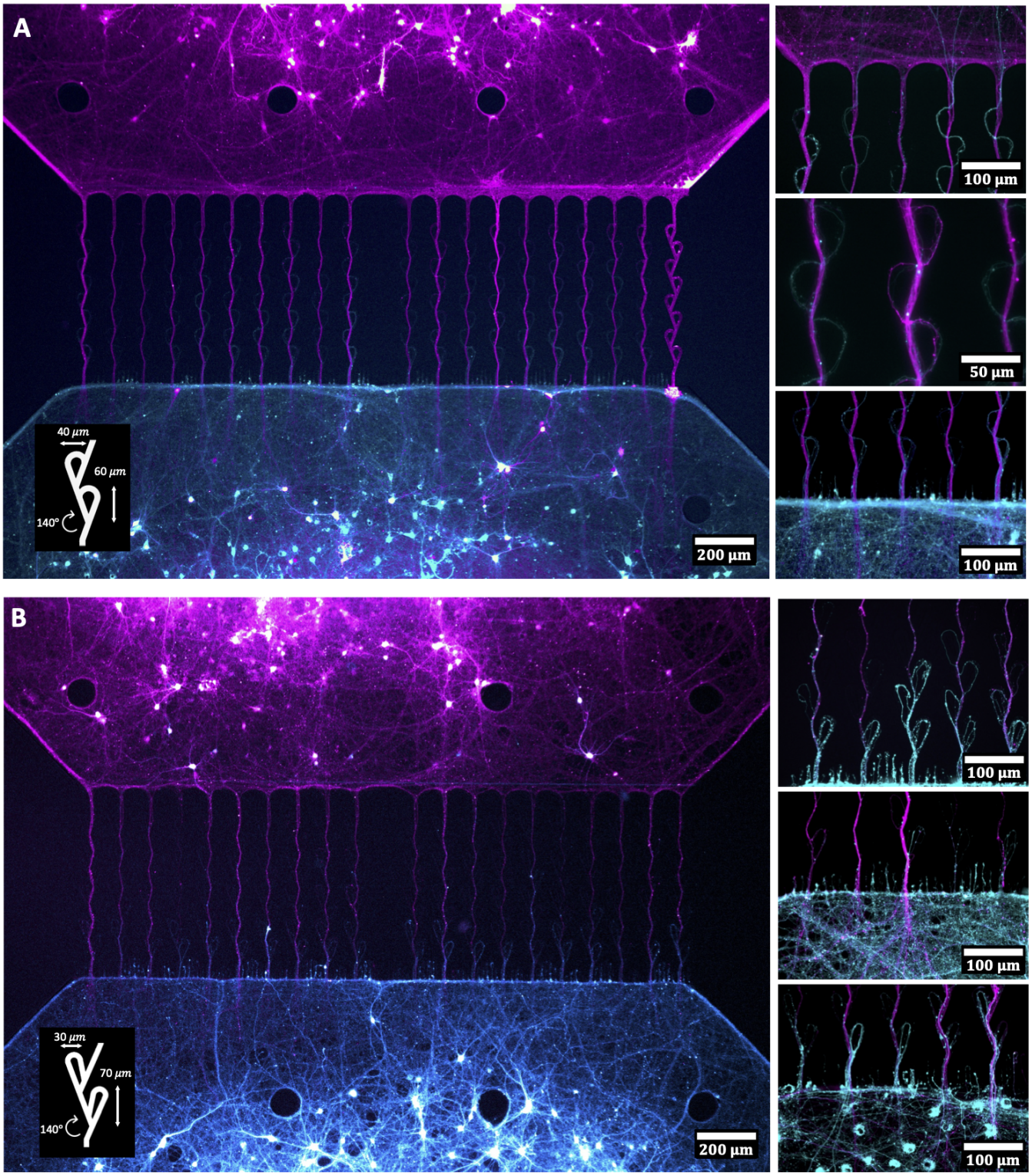

Figure 2 | Images of the selective growth of axons through the Tesla valve inspired microfluidic chips. **(A.)** A loop diameter of $40\,\mu\mathrm{m}$ and height of $60\,\mu\mathrm{m}$ promoted directionality but still allowed for some postsynaptic axons to pass through the channels by exploiting the Tesla valves themselves. **(B.)** Decreasing the diameter to $30\,\mu\mathrm{m}$ and increasing the height to $70\,\mu\mathrm{m}$ effectively redirected the postsynaptic axons back to their chamber of origin within the first 3-4 valves. This effect was found to be stable throughout the culturing period.

also prior to this in both directions, which may be explained by individual network bursts in the two nodes overlapping in time. For the cultures with the most prominent functional connectivity between the nodes, the proportion of feedforward network bursts thereafter increased for a few days until almost all network bursts propagated from the pre- to the postsynaptic node.

As the number of feedforward network bursts increased, the

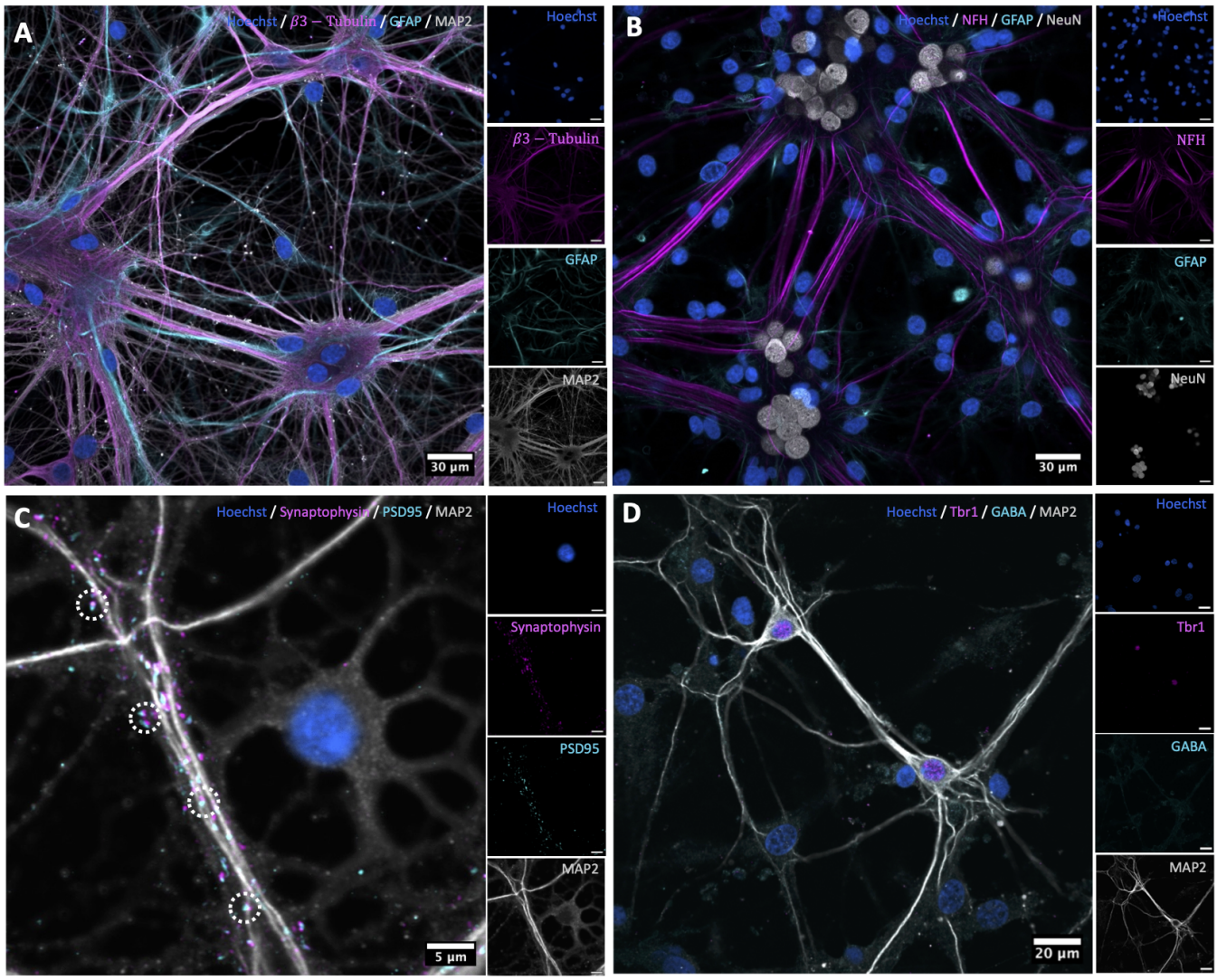

Figure 3 | Immunocytochemistry. **(A.)** The neuronal networks exhibited high degree of clustering and axonal bundling after 14 DIV, demonstrated by the cytoskeletal marker proteins β3-Tubulin and MAP2. **(B.)** Expression of the mature markers Neurofilament Heavy (NFH) and NeuN indicating high degree of maturation after 21 DIV. **(C.)** Colocalization of the pre- and postsynaptic markers synaptophysin and PSD95 at 21 DIV indicating mature synapses. **(D.)** Expression of the glutamatergic receptor Tbr1 and GABA at 21 DIV indicating presence of both excitatory and inhibitory activity.

generation of synchronous activity within the postsynaptic node (i.e., the number of network bursts contained within the postsynaptic chamber) seemed to decrease substantially. However, after a few days the occurrence of feedforward burst propagation seemed to decrease again and the cultures appeared to go back to a state in which most network bursts were contained within the separate nodes. Yet, electrical stimulations of the presynaptic nodes still initiated bursts that clearly spread to the postsynaptic nodes, as will be outlined in the next subsection. This transition could be explained by a trade-off between functional separation and integration in the networks, which has previously been shown to enhance the functional capacity and input representation of modular networks(34). During the initial establishment of structural connections between the two nodes, it is likely that the newly attained afferent input of the postsynaptic node from the presynaptic node caused network depolarizations which effectively synchronized the activity of the two nodes over time. Once the nodes are fully synchronized, there could be mechanisms favouring segregated activity driving the networks back into a state in which most synchronized activity remains within the nodes.

The spike and burst rate of both the two-nodal networks and the single population controls were found to increase with time throughout the duration of the experiments (**Figure 5C**), consistent with previous studies working on *in vitro* neuronal cultures(22, 25, 35). Furthermore, the coherence index, measuring synchrony in the network, showed an initial decline before starting to flatten out. A small increase can be seen in the synchrony around 20 DIV for the two-nodal networks, around the time where two of the networks displayed a significant proportion of forward propagating bursts.

While the nodes in only three out of five microdevices showed signs of functional integration, it is worth noting that the channels used in this study were rather long (700 µm). Previous studies have shown that the dendritic arborization of certain rat cortical neurons can grow to above 300 µm in culture(36), and that a microfluidic design of at least 400 to

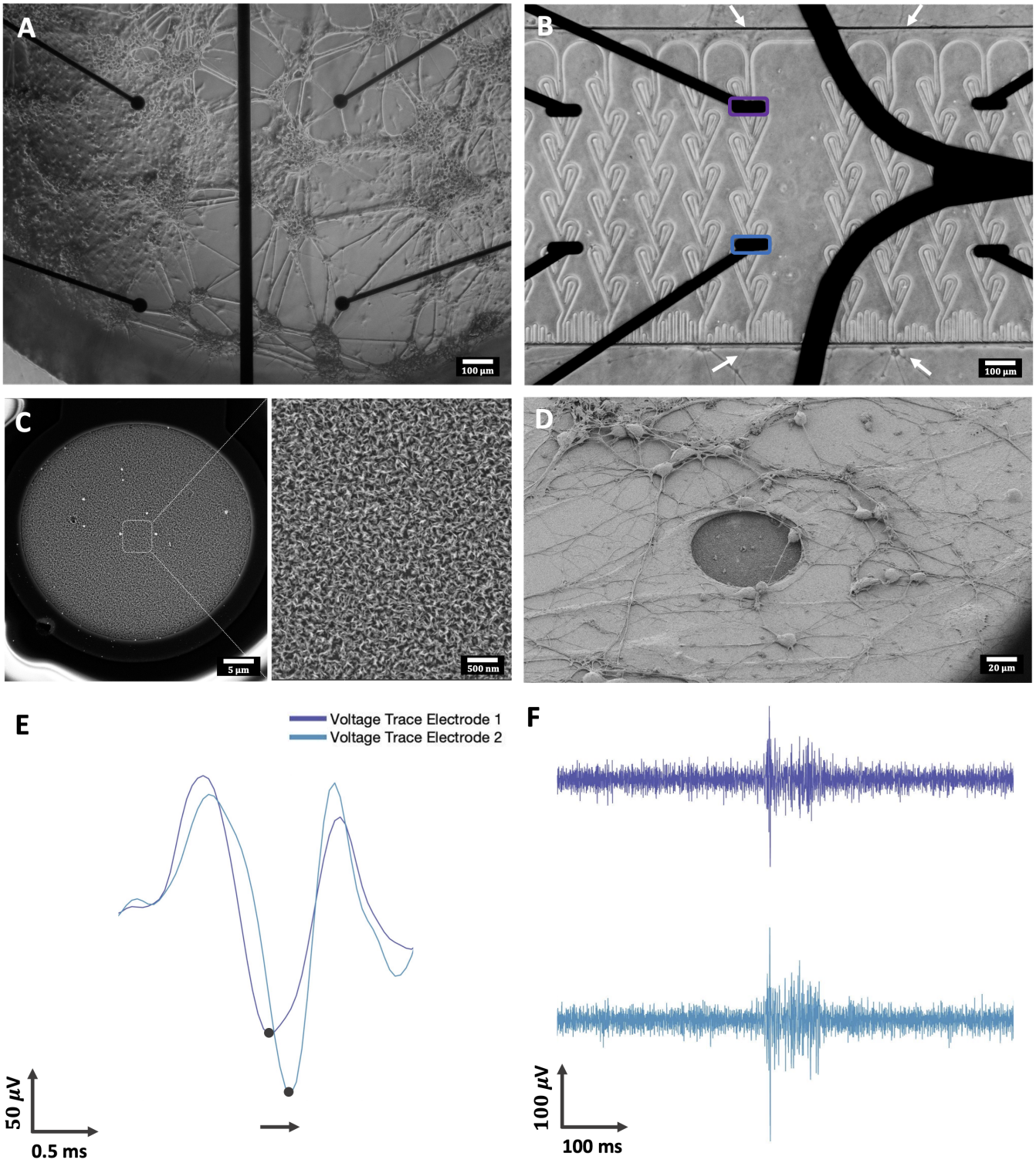

Figure 4 | The microfluidic chips were interfaced with microelectrode arrays for electrophysiological recordings. **(A.)** Micrograph showing clustered networks growing on top four of the microelectrodes. **(B.)** Micrograph demonstrating neurite outgrowth through the microfluidic channels. **(C.)** SEM image of an individual electrode with deposited nanoporous platinum black. **(D.)** SEM image of neurons growing on top of a single microelectrode, demonstrating biocompatibility of the nanoporous electrodes. **(E.)** Voltage traces from two electrodes positioned along a microfluidic channel, demonstrating forward propagation of an action potential. **(F.)** Voltage traces of two electrodes positioned along a microfluidic channel showing the propagation of a single burst.

$450\,\mu\mathrm{m}$ is necessary to avoid dendritic branches from crossing the channels(7, 37). Yet, the ubiquitous expression of GFP/mCherry in this study, capturing all neuritic processes, shows that the Tesla valve design effectively redirected nearly all neurites within three to four valves. With eight valves used in this study, a reduction to half the length ($350\,\mu\mathrm{m}$) might thus still be sufficient to control the afferent connectivity, but could promote more efficient growth through the

channels. Furthermore, it is worth mentioning that Pan *et al.* estimated that a minimum of 100 axons were necessary to reliably transmit a burst from one population to another(15). As shown in **Figure 2**, as much as 15 – 20 individual protrusions can be seen entering the postsynaptic chamber from some channels. With 20 channels connecting the nodes in each microdevice, this should render the networks capable of transmitting bursts between the nodes. However, whether these protrusions were individual axons or collaterals from the same axons is difficult to deduce. Additionally, it is possible that neurites do not grow as readily on the Si_3N_4 used as an insulation layer on the microfluidic MEAs as compared to glass due to surface functionalization characteristics, which could possibly explain why not all the two-nodal chips achieved synchronized activity.

As outlined in the introduction, many studies looking at network development within microfluidic platforms perform structural and/or functional analysis as early as 14 DIV or less. Our study clearly demonstrates the need for more long-term monitoring to evaluate how the microfluidic designs and embedded topographies influence network establishment and activity, preferably up to 28 DIV or longer when the networks have achieved more mature structural connections and established functional connectivity between the nodes.

Electrical Stimulations Induce Feedforward Activity Propagation. Electrical stimulations were applied at 27 DIV to study signal propagation in the two-nodal microdevices. For two nodes that are undirectionally connected, one would expect evoked activity in the presynaptic node to spread to the postsynaptic node, but induced activity in the postsynaptic node to remain within that node. Stimulations were applied to the electrode showing most spontaneous activity prior to stimulations in first the postsynaptic node, followed by the presynaptic node. The stimulations consisted of 60 consecutive $200\,\mu s$ pulses of $800\,mV$ amplitude with a $5\,ms$ interspike interval. As expected, stimulations of the two-nodal networks with no apparent functional connectivity did not induce activity in the opposite neuronal node regardless of the node being stimulated. For the networks that were demonstrated to be functionally connected based on the spontaneously evoked activity, stimulation of the presynaptic node induced a clear response in the postsynaptic node. Stimulation of the postsynaptic node did however not induce any marked responses in the presynaptic node, as illustrated in the raster plots in **Figure 6A**. The peristimulus time histograms showing the average response of one network are shown in **Figure 6B**, demonstrating a consistent forward propagation of network bursts in response to stimulations of the presynaptic node. **Figure 6C** shows a temporal heat map of a single stimulation in both the presynaptic (upper row) and postsynaptic (lower row) node. While the other networks did not exhibit an equally strong propagation of stimulation induced activity (**Figure S8**), both the two other functionally connected networks still showed a clear asymmetry in the response to the stimulation to the pre- and postsynaptic nodes, respectively.

Graph Theoretical Analysis Indicates More Efficient Network Organization in the Two-Nodal Feedforward Network. Functional connectivity matrices and corresponding graphs were calculated based on pairwise mutual information, as detailed in the methods section. **Figures 7A** & **7B** show representative graphs of one two-nodal network and one control network, respectively. As can be seen from the graph representations, the nodes (here referring to individual measurement points) within the two-nodal populations could be effectively delineated into two separate communities, while the single population controls showed more random network organization with less distinguishable communities. While a network with only two communities is shown in **Figure 7B**, several networks also had a higher number of communities with no apparent spatially ordered structure. This is furthermore supported by the plot of the maximized modularity in **Figure 7C**, showing a significant difference between the two-nodal networks and the controls. The difference in the global routing efficiency and characteristic path length of the two-nodal networks and the controls however appeared insignificant.

Notably, the maximized modularity increases again after 20 DIV, indicating more localized activity in the chambers, which is consistent with the bursts ceasing to propagate between the chambers in **Figure 5B**. While this could be a sign of decreased functional connectivity, the results from the stimulations indicate that activity is still readily propagated between the nodes. It is however worth mentioning that the number of measurement points for each network is rather low, which might bias the results. The graph theory package suggests a minimum of 20 nodes for using these tools. While the number of active electrodes in this study was higher than this for all networks, it is still close to the minimum, and conclusions from this analysis should consequently be drawn with care.

Conclusions

*N*euronal assemblies in the brain are connected through highly specific topological projection sequences and hierarchies aiding efficient, directional information processing and computations. Being able to recapitulate aspects of this organization with neuroengineering approaches would enable establishment of more robust model systems for studying structure-function dynamics of neuronal networks *in vitro*. In this study, we have presented a novel microdevice for controlling the afferent connectivity between two neuronal nodes *in vitro* using microchannels with geometries inspired by the Tesla valve design. Furthermore, by combining these devices with viral tools to fluorescently label the neuronal populations in combination with embedded nanoporous microelectrode arrays for functional analysis, we demonstrate the power of our model system for longitudinal studies of structure-function dynamics of such modular neuronal networks. Our results indicate that the networks still undergo significant structural alterations beyond 3 weeks *in vitro*, and that the number of network bursts spanning both nodes increases over time. Furthermore, structurally connected nodes

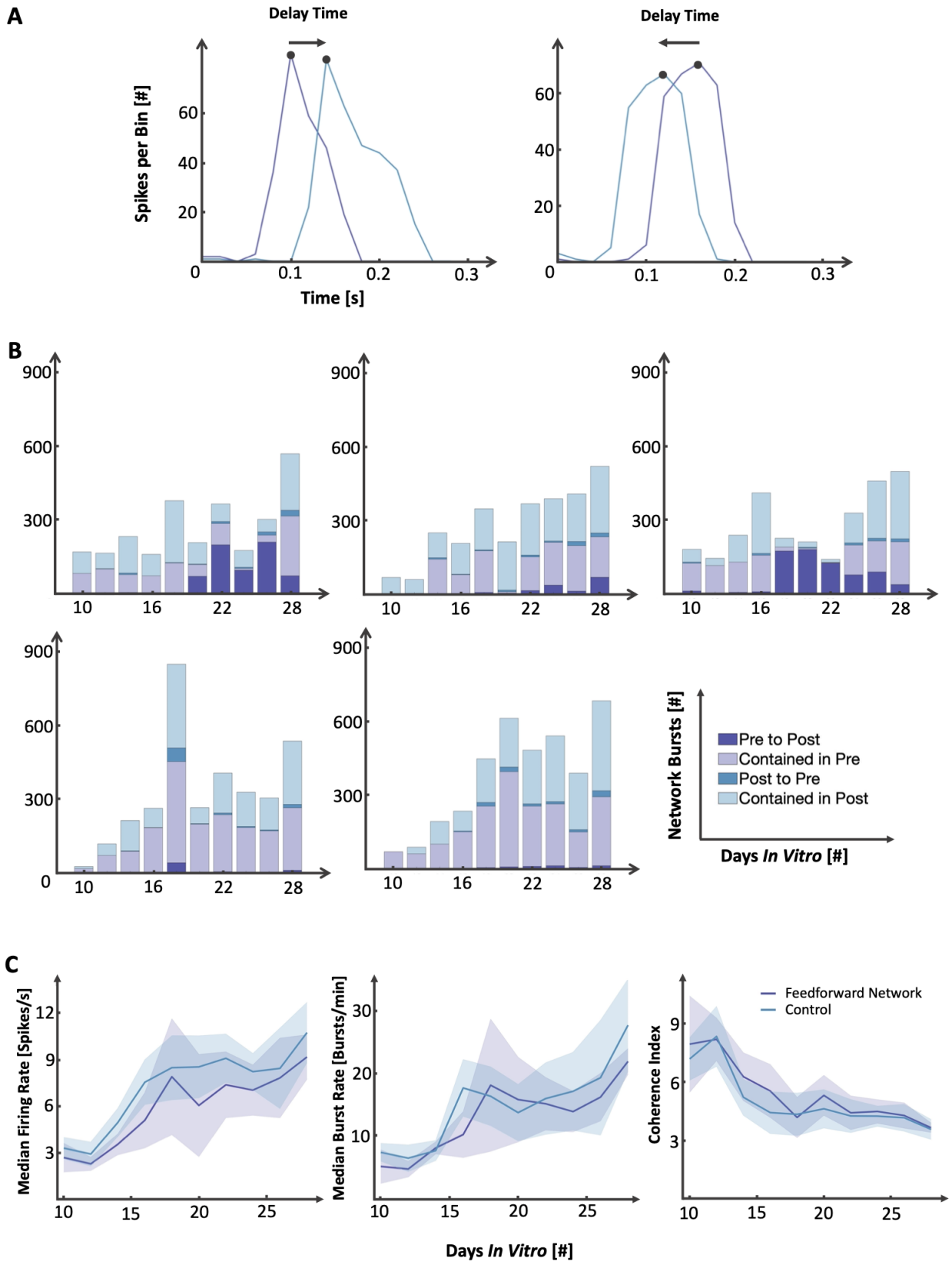

Figure 5 | Development of spontaneous network activity. **(A.)** Tuning curves of individual network bursts in both nodes were plotted and used to determine the direction of activity propagation. **(B.)** Histograms for each node showing the number of network bursts being contained within the individual nodes, as well as propagated between them for each recording. Three two-nodal networks showed clear signs of functional connectivity with feedforward propagating bursts. **(C.)** Firing rate and burst rate increased comparably over time for both the two-nodal networks and the controls. The coherence index showed an initial decline, before flattening out around 14 DIV.

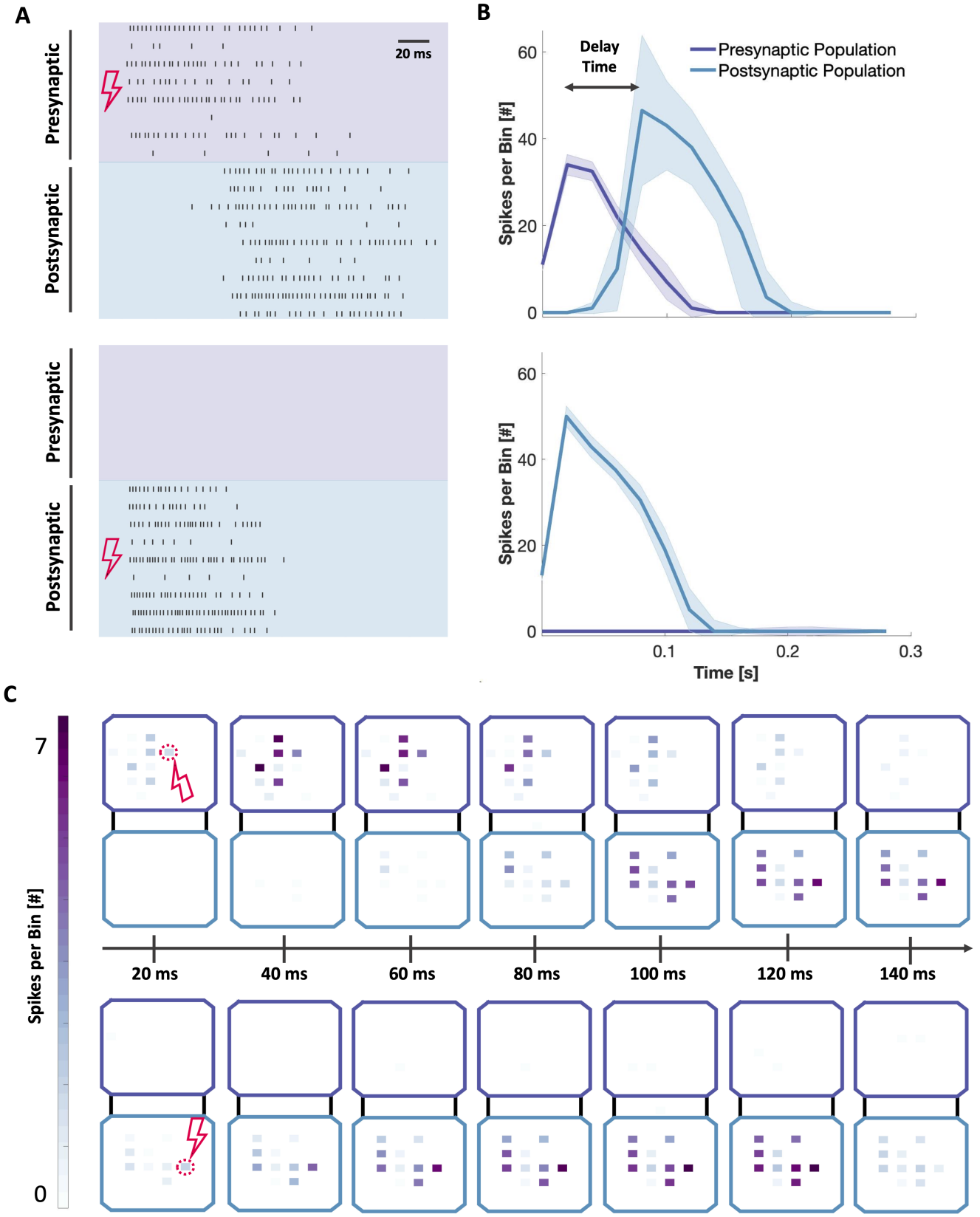

Figure 6 | Illustration of response to electrical stimulations. **(A)** Raster plots showing propagation of a single network burst initiated by stimulation of the presynaptic and postsynaptic nodes, respectively. **(B)** Peristimulus time histograms showing the average response of 60 stimulations on each of the two nodes. As can be clearly seen, stimulations of the presynaptic node induced a delayed response in the postsynaptic node, but nearly no response was induced in the presynaptic node upon stimulation of the postsynaptic node. **(C)** Heat maps showing the binned $(20\,\mathrm{ms})$ instantaneous firing of each active electrode in the $140\,\mathrm{ms}$ following a stimulation in the pre- and postsynaptic nodes, respectively, further illustrating the spread of activity from the pre- to the postsynaptic node, but not vice versa.

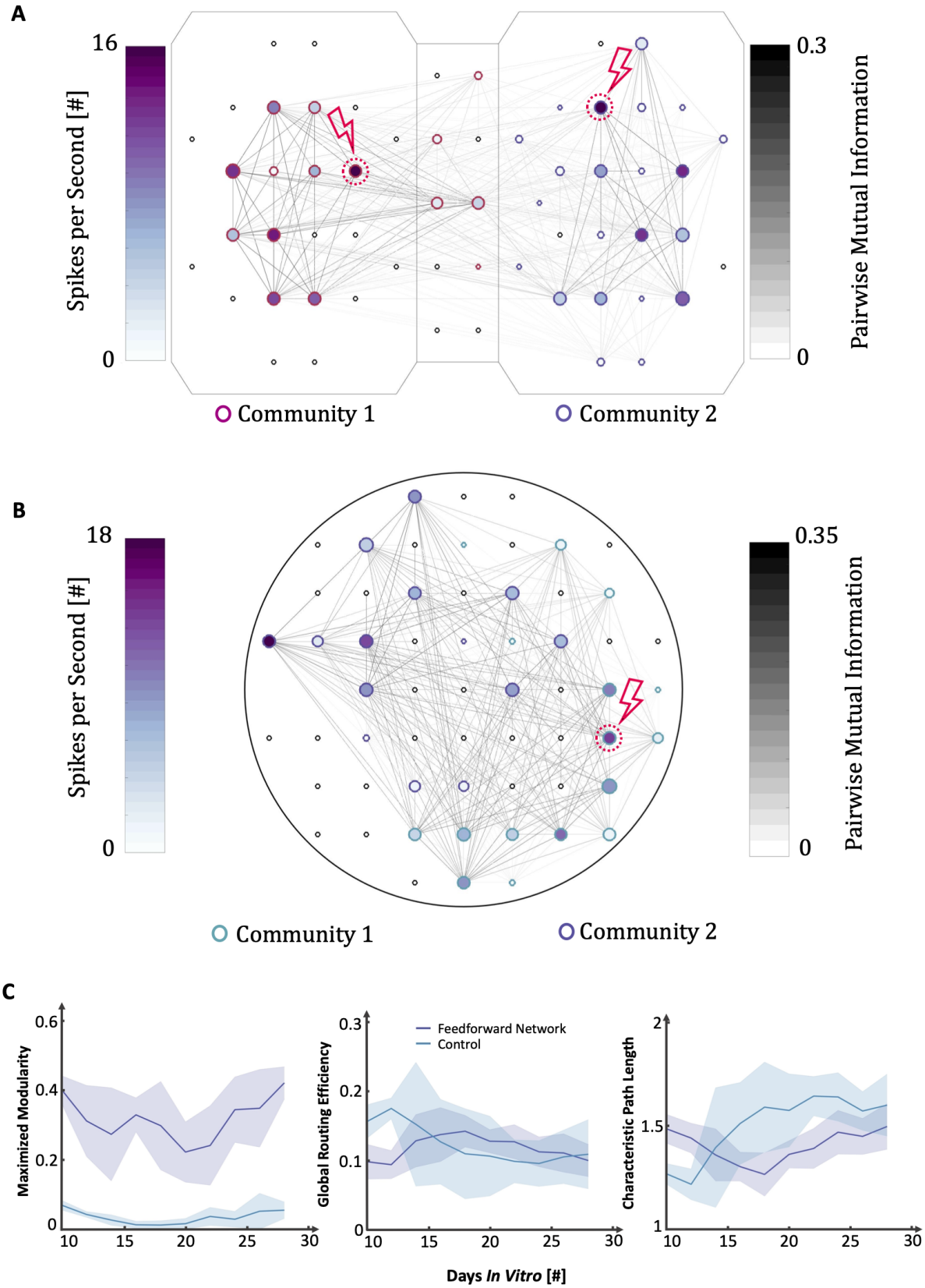

Figure 7 | Graph Theoretical Analysis. **(A.)** Representative graph showing one of the two-nodal networks. Node colour represents firing frequency, edge colour the pairwise mutual information, node size the PageRank centrality and node edge colour the community belonging. **(B.)** Representative graph showing one of the control networks, demonstrating less clearly distinguishable modules. **(C.)** Plots showing that the maximized modularity is significantly higher for the two-nodal networks, while global routing efficiency and characteristic path length are more comparable in size.

readily propagate activity evoked by electrical stimulations in a feedforward fashion. While only 60 % of the two-nodal cultures reached functional connectivity during the time span of this study, the high efficacy of the design at promoting unidirectional axonal growth indicates that a reduction of channel lengths might provide more efficient growth of axons through the channels without compromising the unidirectionality. This technology can be utilized to build model systems resembling the mesoscale architectural motifs found in the brain to further advance our understanding of how such networks organize, compute, adapt and represent information in both health and disease.

AUTHOR CONTRIBUTIONS

The author contributions follow the CRediT system. **NWH**: Conceptualization, Methodology, Software, Investigation (chip design & manufacturing, cell experiments, electrophysiology, formal analysis), Writing – Original Draft, Visualization. **ÅBT**: Investigation (immunocytochemistry and confocal microscopy), Writing – Review & Editing. **PS, AS, IS**: Conceptualization, Methodology, Writing – Review & Editing, Funding acquisition.

ACKNOWLEDGEMENTS

NTNU Enabling technologies and Health Mid-Norway are acknowledged for funding this research. The Research Council of Norway is acknowledged for the support to the Norwegian Micro- and Nano-Fabrication Facility, NorFab, project number 295864.

We would like to thank Dr. Rajeevkumar Nair Raveendran at the Viral Vector Core Facility, Kavli Institute for systems neuroscience, for designing and preparing the AAV2/1 viruses used for structural analysis, Prof. Michela Chiappalone and Prof. Sergio Martinoia, University of Genova for generously providing the scripts for the Precise Timing Spike Detection algorithm and the logISI burst detection, and Edevard Hvide MSc for acquisition of the SEM image in **Figure 2D**. We acknowledge Senior Engineer Astrid Bjørkøy and the Center for Advanced Microscopy (CAM) at the Department of Physics, Faculty of Natural Sciences, NTNU for technical assistance and access to confocal microscopy infrastructure.

COMPETING FINANCIAL INTERESTS

The authors declare that the research was conducted in the absence of any commercial or financial relationships that could be construed as a potential conflict of interest.

Bibliography

1. A. M. Taylor, S. W. Rhee, C. H. Tu, D. H. Cribbs, C. W. Cotman, and N. L. Jeon. Microfluidic multicompartment device for neuroscience research. *Langmuir*, 19(5):1551–1556, 2003. ISSN 0743-7463 (Print) 0743-7463. doi: 10.1021/la026417v.
2. L. Luo. Architectures of neuronal circuits. *Science*, 373(6559):eabg7285, 2021. doi: 10.1126/science.abg7285.
3. G. S. Withers, C. D. James, C. E. Kingman, H. G. Craighead, and G. A. Banker. Effects of substrate geometry on growth cone behavior and axon branching. *J Neurobiol*, 66(11):1183–94, 2006. ISSN 0022-3034 (Print) 0022-3034. doi: 10.1002/neu.20298.
4. E. W. Dent, S. L. Gupton, and F. B. Gertler. The growth cone cytoskeleton in axon outgrowth and guidance. *Cold Spring Harb Perspect Biol*, 3(3), 2011. ISSN 1943-0264. doi: 10.1101/cshperspect.a001800.
5. G. Gangatharan, S. Schneider-Maunoury, and M. A. Breau. Role of mechanical cues in shaping neuronal morphology and connectivity. *Biol Cell*, 110(6):125–136, 2018. ISSN 0248-4900. doi: 10.1111/boc.201800003.
6. J. M. Peyrin, B. Deleglise, L. Saias, M. Vignes, P. Gougis, S. Magnifico, S. Betuing, M. Pietri, J. Caboche, P. Vanhoutte, J. L. Viovy, and B. Brugg. Axon diodes for the reconstruction of oriented neuronal networks in microfluidic chambers. *Lab Chip*, 11(21):3663–73, 2011. ISSN 1473-0189. doi: 10.1039/c1lc20014c.
7. E. Malishev, A. Pimashkin, A. Gladkov, Y. Pigareva, A. Bukatin, V. Kazantsev, I. Mukhina, and M. Dubina. Microfluidic device for unidirectional axon growth. *Journal of Physics: Conference Series*, 643, 2015.
8. J. le Feber, W. Postma, E. de Weerd, M. Weusthof, and W. L. Rutten. Barbed channels enhance unidirectional connectivity between neuronal networks cultured on multi electrode arrays. *Front Neurosci*, 9:412, 2015. ISSN 1662-4548 (Print) 1662-453x. doi: 10.3389/fnins.2015.00412.
9. A. Gladkov, Y. Pigareva, D. Kutyina, V. Kolpakov, A. Bukatin, I. Mukhina, V. Kazantsev, and A. Pimashkin. Design of cultured neuron networks in vitro with predefined connectivity using asymmetric microfluidic channels. *Sci Rep*, 7(1):15625, 2017. ISSN 2045-2322. doi: 10.1038/s41598-017-15506-2.
10. Y. Pigareva, A. Gladkov, V. Kolpakov, I. Mukhina, A. Bukatin, V. B. Kazantsev, and A. Pimashkin. Experimental platform to study spiking pattern propagation in modular networks in vitro. *Brain Sci*, 11(6), 2021. ISSN 2076-3425 (Print) 2076-3425. doi: 10.3390/brainsci11060717.
11. S. Na, M. Kang, S. Bang, D. Park, J. Kim, S. J. Sim, S. Chang, and N. L. Jeon. Microfluidic neural axon diode. *Technology*, 4(4):240–248, 2016.
12. P. M. Holloway, G. I. Hallinan, M. Hegde, S. I. R. Lane, K. Deinhardt, and J. West. Asymmetric confinement for defining outgrowth directionality. *Lab Chip*, 19(8):1484–1489, 2019. ISSN 1473-0189. doi: 10.1039/c9lc00078j.
13. R. Renault, J. B. Durand, J. L. Viovy, and C. Villard. Asymmetric axonal edge guidance: a new paradigm for building oriented neuronal networks. *Lab Chip*, 16(12):2188–91, 2016. ISSN 1473-0189. doi: 10.1039/c6lc00479b.
14. M. J. Mahoney, R. R. Chen, J. Tan, and W. M. Saltzman. The influence of microchannels on neurite growth and architecture. *Biomaterials*, 26(7):771–8, 2005. ISSN 0142-9612 (Print) 0142-9612. doi: 10.1016/j.biomaterials.2004.03.015.
15. L. Pan, S. Alagapan, E. Franca, S. S. Leondopulos, T. B. DeMarse, G. J. Brewer, and B. C. Wheeler. An in vitro method to manipulate the direction and functional strength between neural populations. *Front Neural Circuits*, 9:32, 2015. ISSN 1662-5110. doi: 10.3389/fncir.2015.00032.
16. Nikola Tesla. Valvular conduit, 1920.
17. Fred K. Forster, Ronald L. Bardell, Martin A. Afromowitz, Nigel R. Sharma, and Alan Blanchard. Design, fabrication and testing of fixed-valve micro-pumps. *Proceedings of the ASME Fluids Engineering Division*, 234, 1995.
18. R. van de Wijdeven, O. H. Ramstad, U. S. Bauer, Ø Halaas, A. Sandvig, and I. Sandvig. Structuring a multi-nodal neural network in vitro within a novel design microfluidic chip. *Biomed Microdevices*, 20(1):9, 2018. ISSN 1387-2176. doi: 10.1007/s10544-017-0254-4.
19. R. van de Wijdeven, O. H. Ramstad, V. D. Valderhaug, P. Köllensperger, A. Sandvig, I. Sandvig, and Ø Halaas. A novel lab-on-chip platform enabling axotomy and neuromodulation in a multi-nodal network. *Biosens Bioelectron*, 140:111329, 2019. ISSN 0956-5663. doi: 10.1016/j.bios.2019.111329.
20. K. N. Richter, N. H. Revelo, K. J. Seitz, M. S. Helm, D. Sarkar, R. S. Saleeb, E. D'Este, J. Eberle, E. Wagner, C. Vogl, D. F. Lazaro, F. Richter, J. Coy-Vergara, G. Coceano, E. S. Boyden, R. R. Duncan, S. W. Hell, M. A. Lauterbach, S. E. Lehnart, T. Moser, T. F. Outeiro, P. Rehling, B. Schwappach, I. Testa, B. Zapiec, and S. O. Rizzoli. Glyoxal as an alternative fixative to formaldehyde in immunostaining and super-resolution microscopy. *Embo j*, 37(1):139–159, 2018. ISSN 0261-4189 (Print) 0261-4189. doi: 10.15252/embj.201695709.
21. A. Maccione, M. Gandolfo, P. Massobrio, A. Novellino, S. Martinoia, and M. Chiappalone. A novel algorithm for precise identification of spikes in extracellularly recorded neuronal signals. *J Neurosci Methods*, 177(1):241–9, 2009. ISSN 0165-0270 (Print) 0165-0270. doi: 10.1016/j.jneumeth.2008.09.026.
22. V. Pasquale, S. Martinoia, and M. Chiappalone. A self-adapting approach for the detection of bursts and network bursts in neuronal cultures. *J Comput Neurosci*, 29(1-2):213–229, 2010. ISSN 0929-5313. doi: 10.1007/s10827-009-0175-1.
23. L. L. Bologna, V. Pasquale, M. Garofalo, M. Gandolfo, P. L. Baljon, A. Maccione, S. Martinoia, and M. Chiappalone. Investigating neuronal activity by spycode multi-channel data analyzer. *Neural Netw*, 23(6):685–97, 2010. ISSN 0893-6080. doi: 10.1016/j.neunet.2010.05.002.
24. X. J. Wang. Pacemaker neurons for the theta rhythm and their synchronization in the septohippocampal reciprocal loop. *J Neurophysiol*, 87(2):889–900, 2002. ISSN 0022-3077 (Print) 0022-3077. doi: 10.1152/jn.00135.2001.
25. D. A. Wagenaar, J. Pine, and S. M. Potter. An extremely rich repertoire of bursting patterns during the development of cortical cultures. *BMC Neurosci*, 7:11, 2006. ISSN 1471-2202. doi: 10.1186/1471-2202-7-11.
26. D. A. Wagenaar and S. M. Potter. Real-time multi-channel stimulus artifact suppression by local curve fitting. *J Neurosci Methods*, 120(2):113–20, 2002. ISSN 0165-0270 (Print) 0165-0270. doi: 10.1016/s0165-0270(02)00149-8.
27. Benjamin Kraus. Spike raster plot, 2022.
28. Ameya Deoras. Customizable heat maps, 2022.
29. N. M. Timme and C. Lapish. A tutorial for information theory in neuroscience. *eNeuro*, 5(3), 2018. ISSN 2373-2822. doi: 10.1523/eneuro.0052-18.2018.
30. M. Rubinov and O. Sporns. Complex network measures of brain connectivity: uses and interpretations. *Neuroimage*, 52(3):1059–69, 2010. ISSN 1053-8119. doi: 10.1016/j.neuroimage.2009.10.003.
31. Jonathan C. Lansey. Beautiful and distinguishable line colors + colormap, 2022.
32. Stephen23. Colorbrewer: Attractive and distinctive colormaps, 2022.
33. Cynthia A. Brewer, Geoffrey W. Hatchard, and Mark A. Harrower. Colorbrewer in print: A catalog of color schemes for maps. *Cartography and Geographic Information Science*, 30(1):5–32, 2003.
34. O. Levy, N. E. Ziv, and S. Marom. Enhancement of neural representation capacity by modular architecture in networks of cortical neurons. *Eur J Neurosci*, 35(11):1753–60, 2012. ISSN 0953-816x. doi: 10.1111/j.1460-9568.2012.08094.x.
35. E. Maeda, H. P. Robinson, and A. Kawana. The mechanisms of generation and propagation of synchronized bursting in developing networks of cortical neurons. *J Neurosci*, 15(10):6834–45, 1995. ISSN 0270-6474 (Print) 0270-6474. doi: 10.1523/jneurosci.15-10-06834.1995.
36. A. R. Kriegstein and M. A. Dichter. Morphological classification of rat cortical neurons in cell culture. *J Neurosci*, 3(8):1634–47, 1983. ISSN 0270-6474 (Print) 0270-6474. doi: 10.1523/jneurosci.03-08-01634.1983.
37. A. M. Taylor, M. Blurton-Jones, S. W. Rhee, D. H. Cribbs, C. W. Cotman, and N. L. Jeon. A microfluidic culture platform for cns axonal injury, regeneration and transport. *Nat Methods*, 2(8):599–605, 2005. ISSN 1548-7091 (Print) 1548-7091. doi: 10.1038/nmeth777.

Supplementary Materials

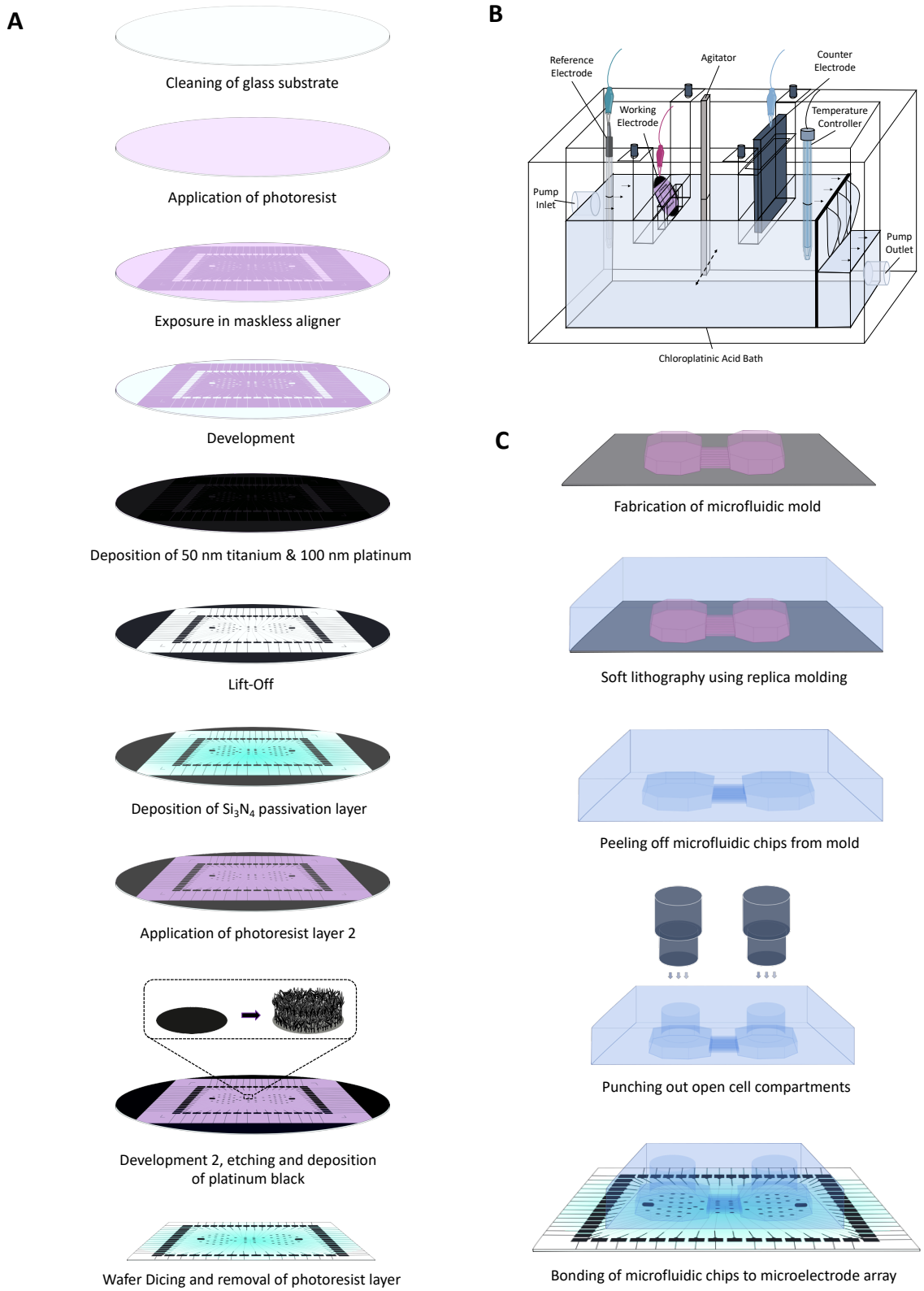

Figure S1 | Schematics of fabrication process, as described in the methods section of the main paper. **(A.)** Fabrication of microelectrode arrays. **(B.)** Setup for electrochemical deposition of nanoporous platinum black. **(C.)** Fabrication of microfluidics chips.

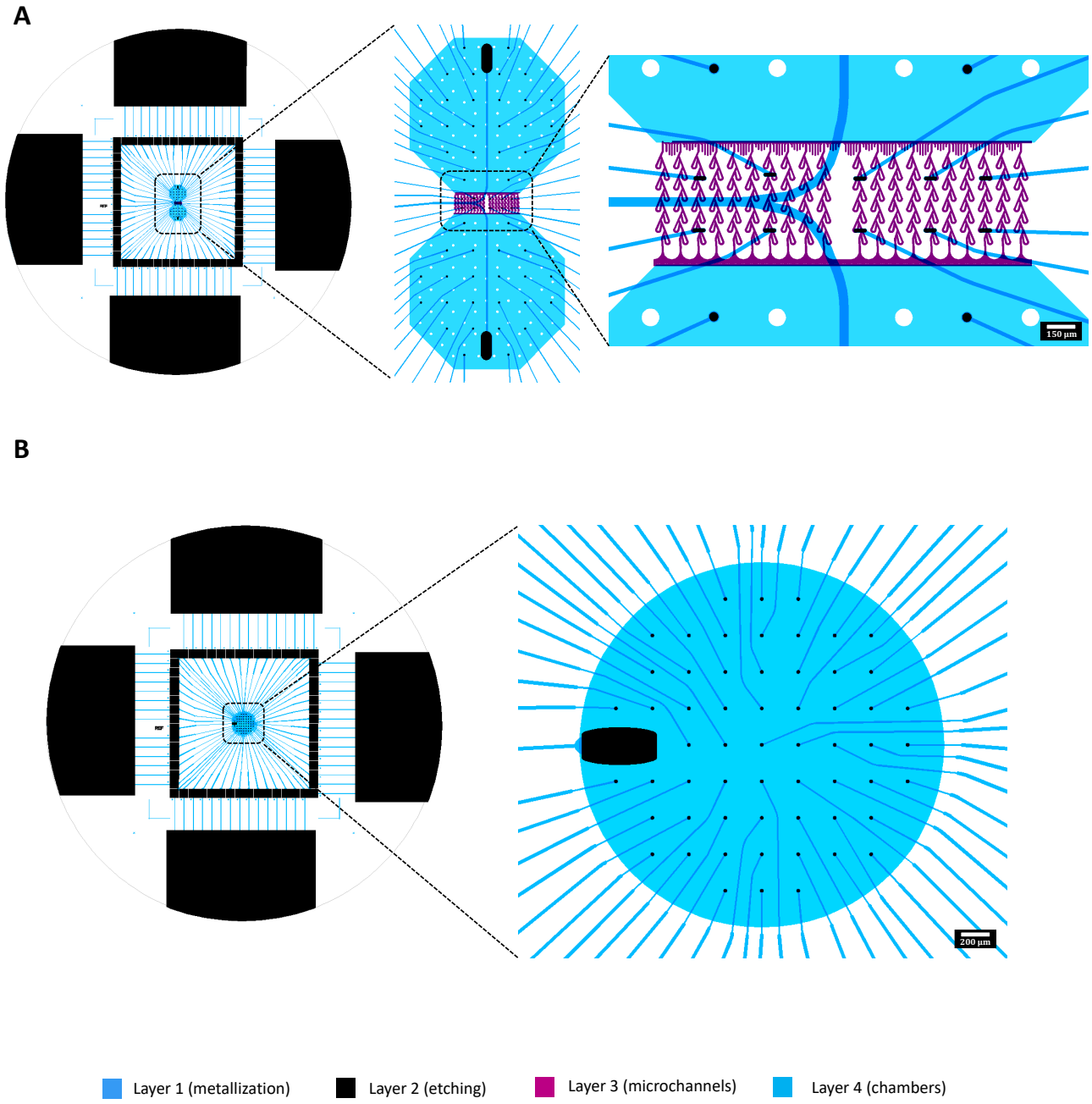

Figure S2 | CAD designs of **(A.)** the two-nodal microfluidic platform and **(B.)** the single population control platform. Layer 1 is the design for metallization, layer 2 for the etch mask, layer 3 for the microfluidic channels and layer 4 for the cell compartments.

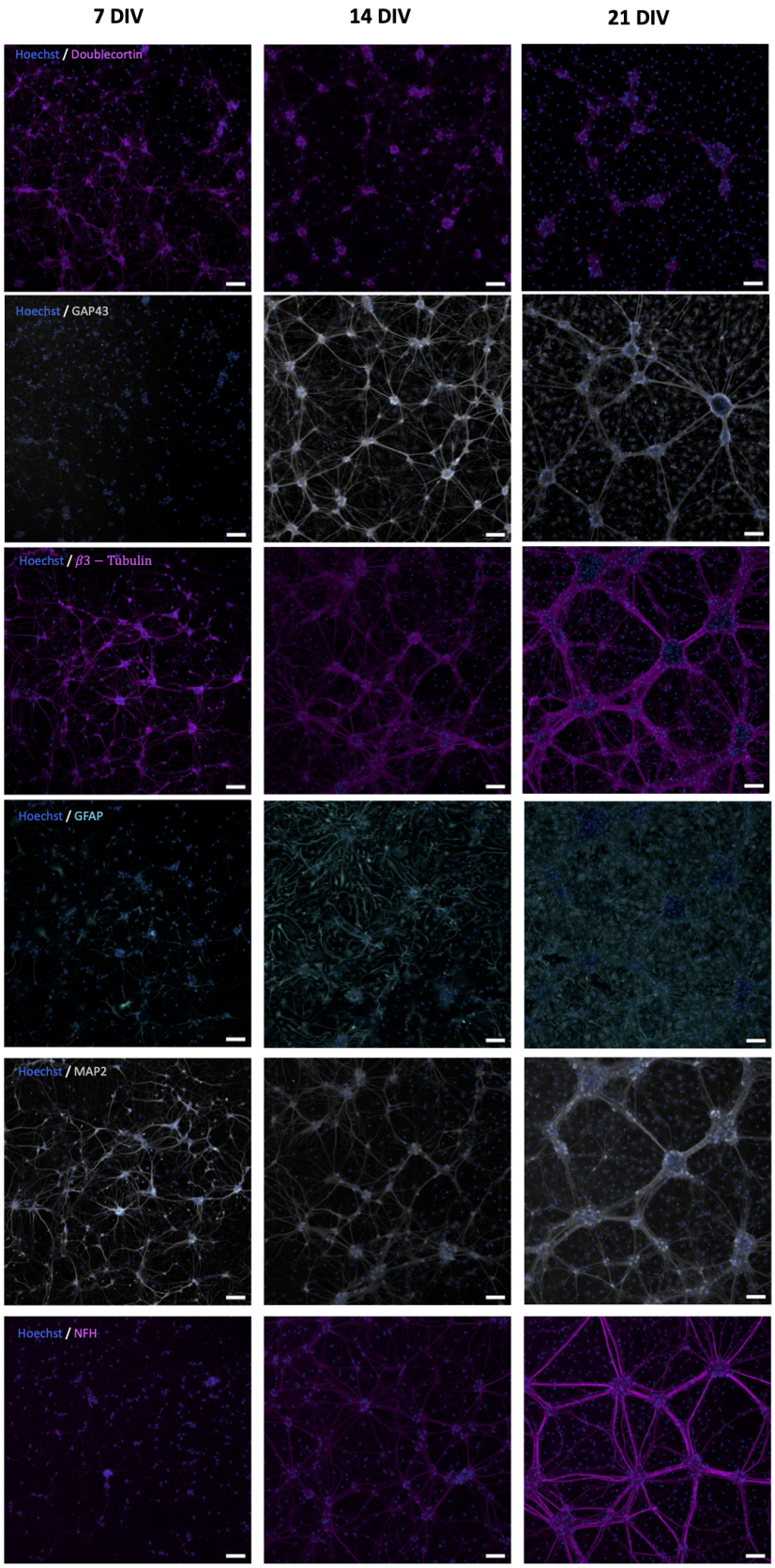

Figure S3 | Immunocytochemistry showing longitudinal expression of doublecortin and GAP43 (neurodevelopmental markers), β3-Tubulin and MAP2 (cytoskeletal markers), NFH (mature cytoskeletal marker) and GFAP (astrocytic marker). Scale bars: $30\,\mu\mathrm{m}$.

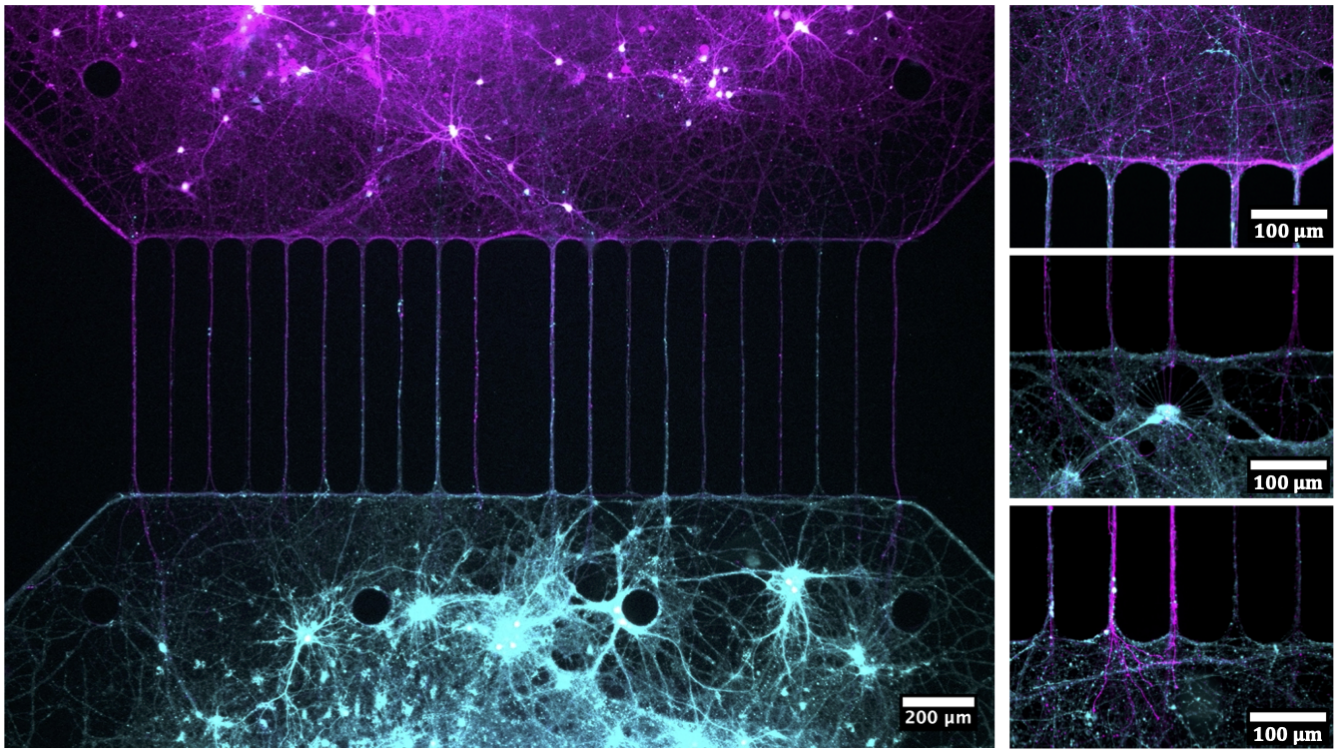

Figure S4 | Neuronal cultures transfected with AAV2/1 with a CMV ubiquitous promoter for expression of GFP/mCherry in microfluidic controls with bidirectional channels. The figure illustrates the clear bidirectional growth in the channels when no geometrical constraints are used to promote unidirectional axonal growth.

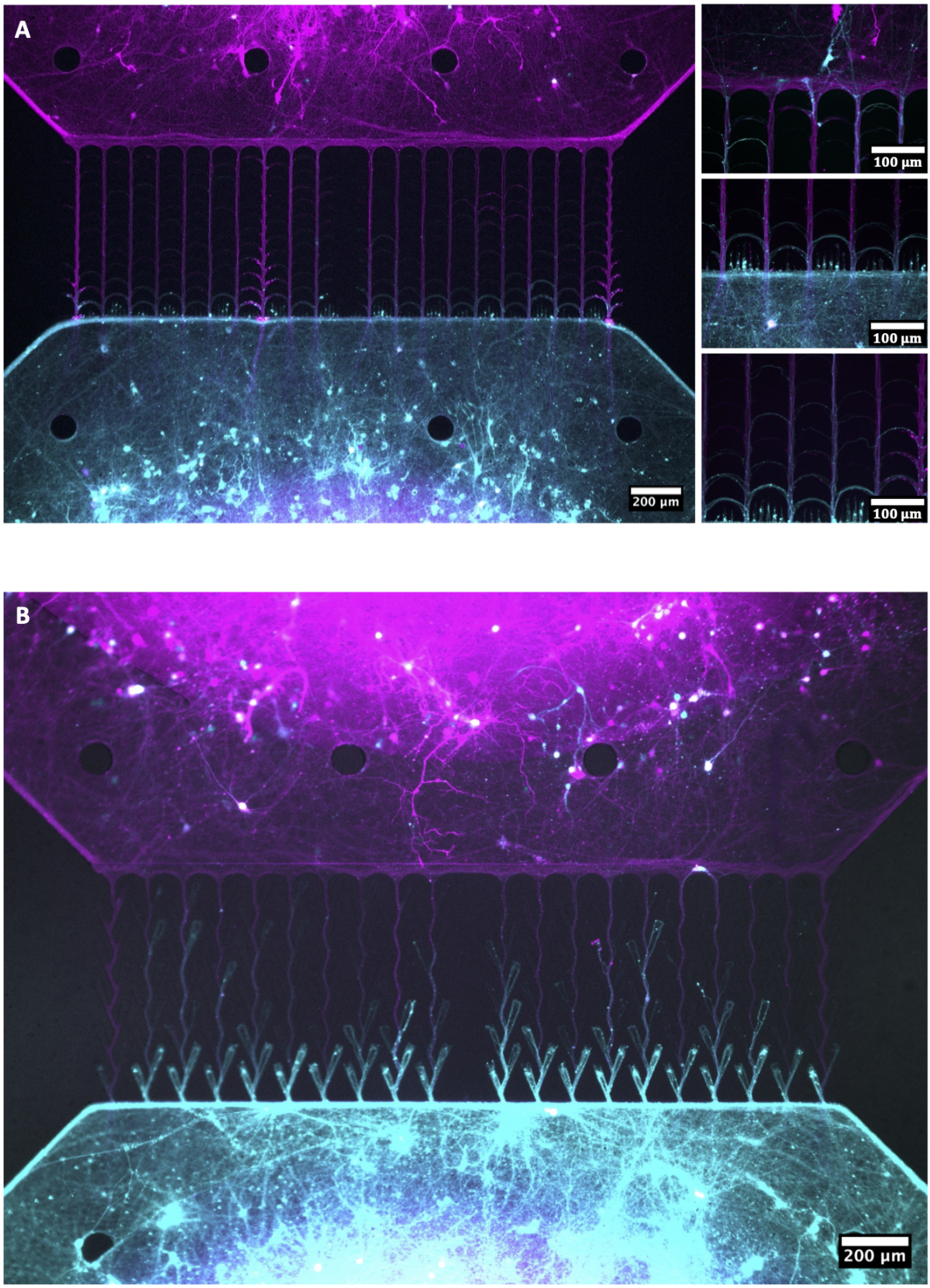

Figure S5 | Neuronal cultures transfected with AAV2/1 with a CMV ubiquitous promoter for expression of GFP/mCherry seeded in: **(A.)** U-shapes channels, as pioneered by Renault *et al.* **(B.)** Spine structures as previously described by Gladkov *et al.*

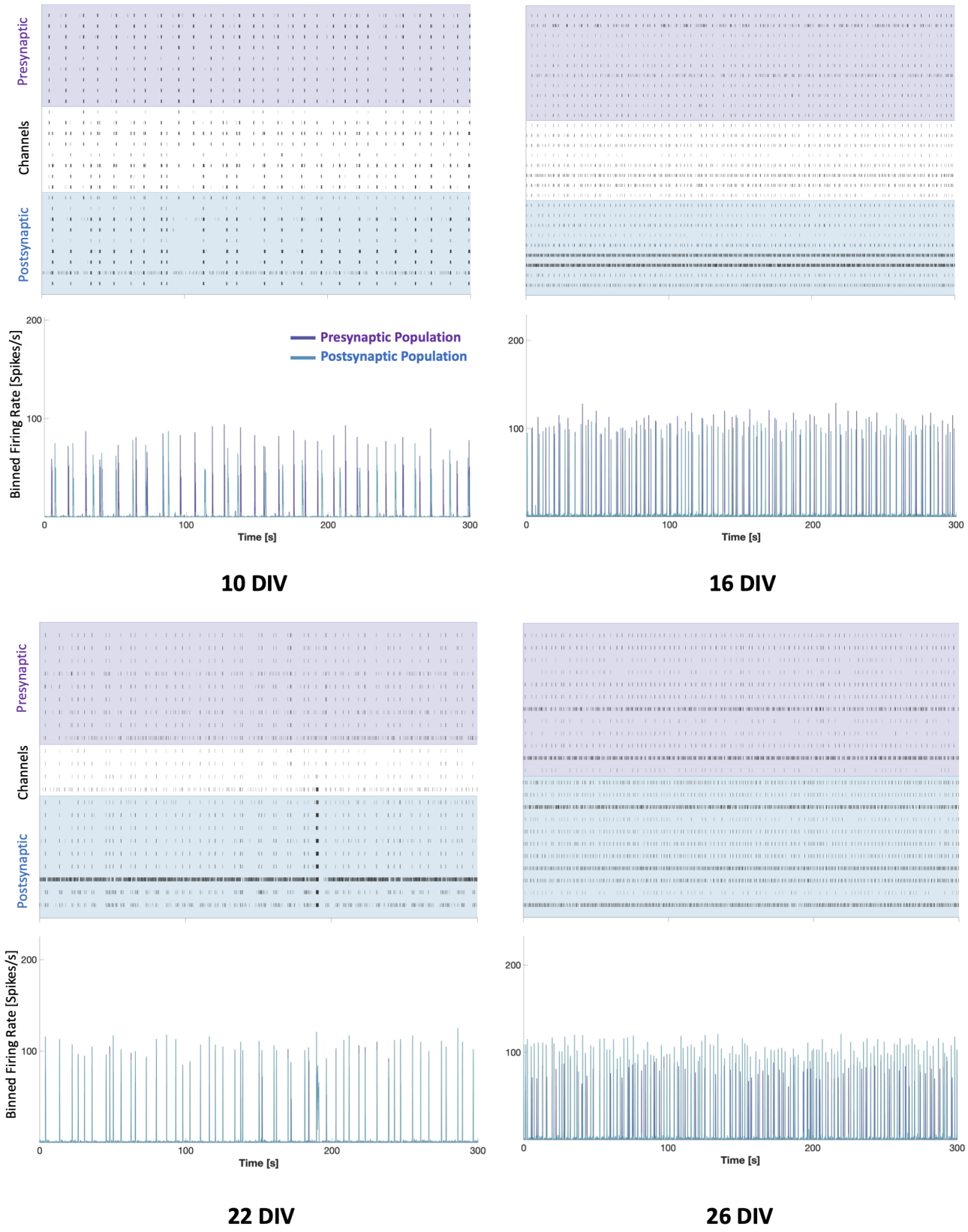

Figure S6 | Raster Plots, and $50\,\mathrm{ms}$ binned activity plots showing the development in spiking activity for one representative two-nodal network at 10, 16, 22 and 26 DIV, demonstrating the gradual increase in correlated activity between the two nodes before the nodes exhibit more separated activity again at DIV 26.

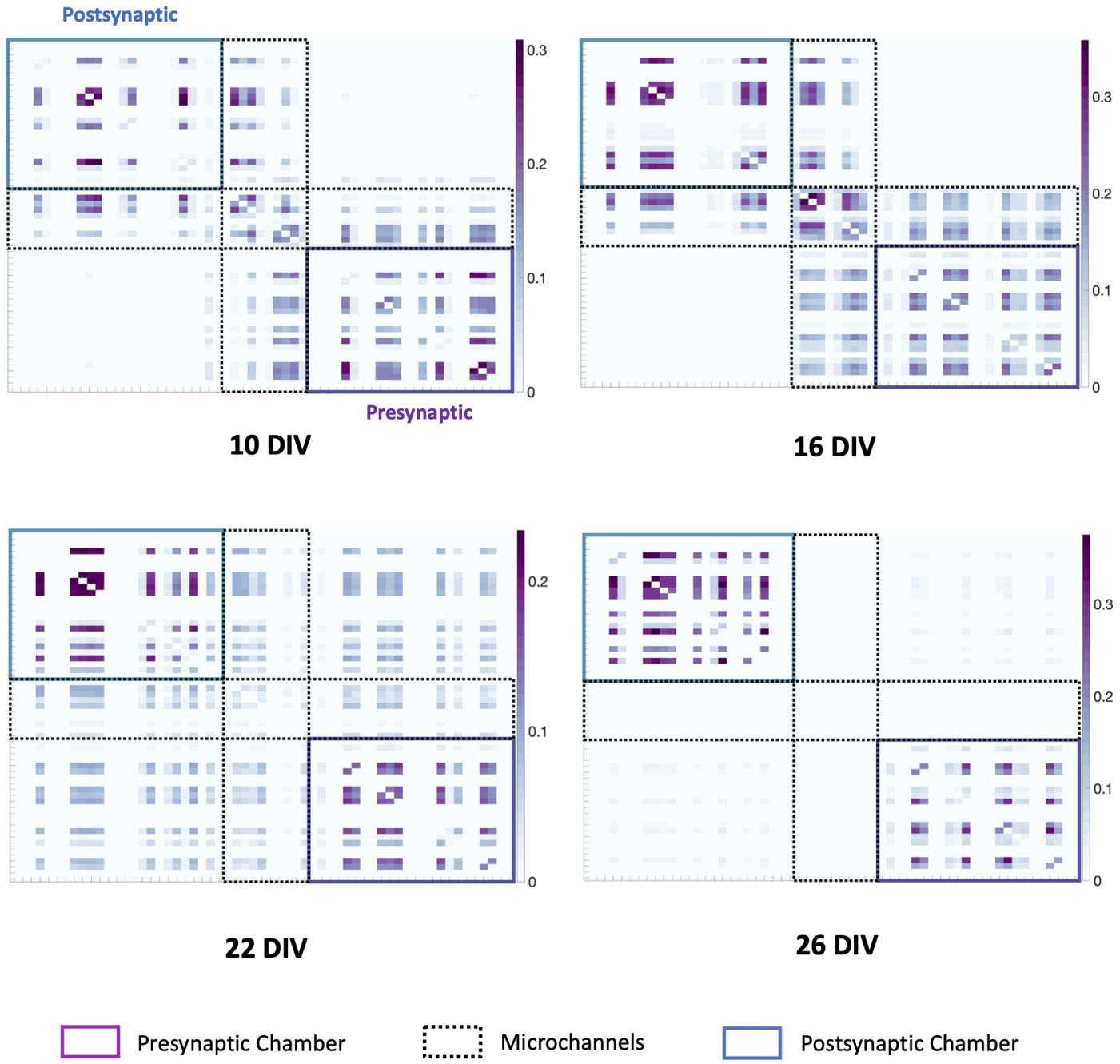

Figure S7 | Functional connectivity/adjacency matrices showing the development in functional connectivity for one two-nodal network at 10, 16, 22 and 26 DIV, demonstrating the gradually increasing functional connectivity as the network matures.

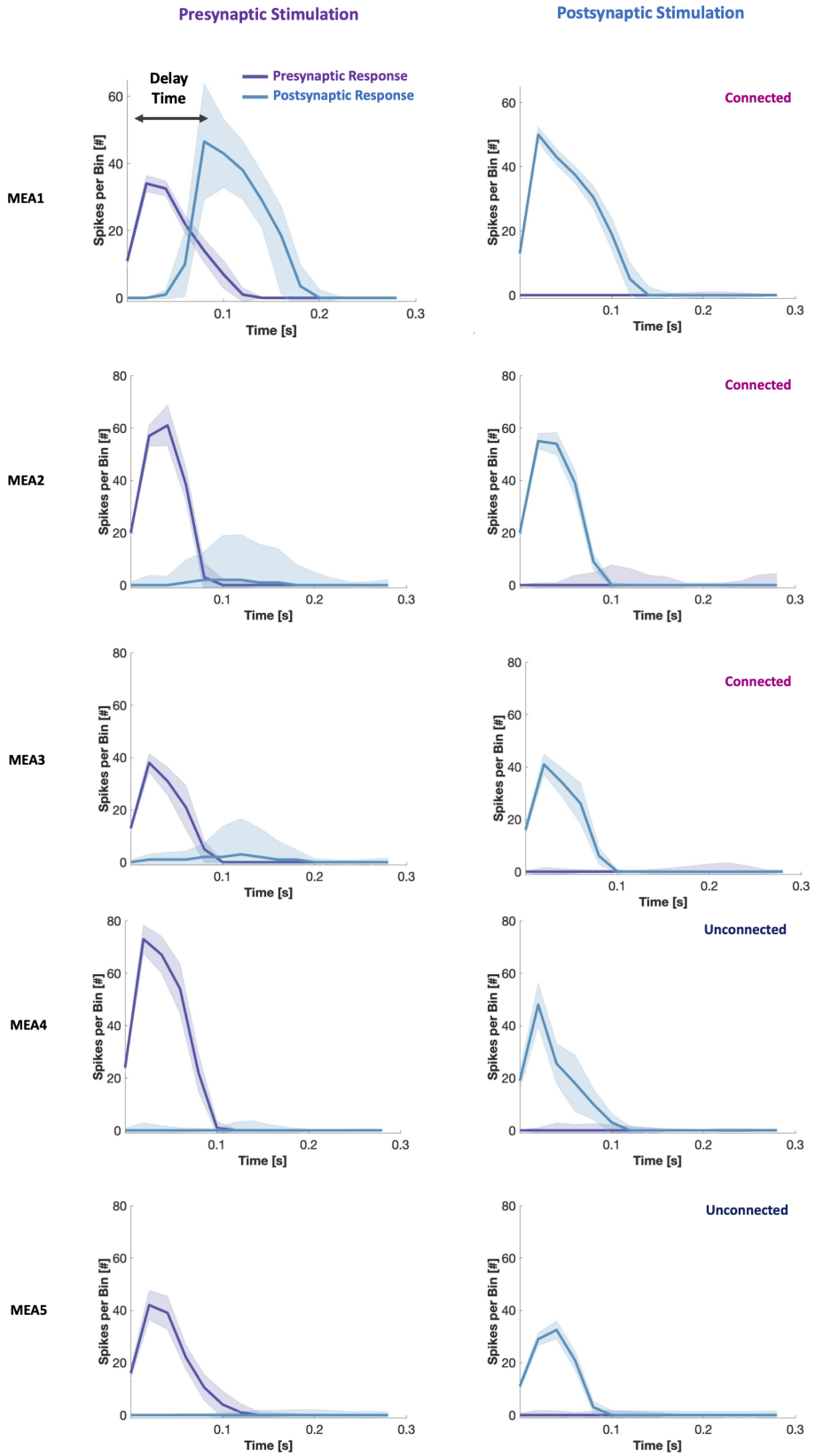

Figure S8 | Peristimulus time histograms for the five two-nodal cultures. As can be seen from the graphs, three of the cultures showed a clear spread of activity from the pre- to the postsynaptic population when the presynaptic population was stimulated, while either no or a minimal response was observed in the presynaptic population when the postsynaptic population was stimulated. Two cultures did not appear to have any functional connectivity.

Protocol for SEM Fixation and Imaging

For cell fixation, all the cell media were removed, and the cultures rinsed with PBS solution two times to remove debris. Consecutively, the PBS was replaced by 2.5% glutaraldehyde in Sorensen´s phosphate buffer ($0.1\,\mathrm{mol}$, pH 7.2), barely covering the cells. The cells were incubated in the buffer at $4\,^{\circ}\mathrm{C}$ overnight. Thereafter, a serial dehydration step was conducted to remove all water from the specimens, in steps of 30%, 50%, 70%, 90% and 100% ethanol with $10\,\mathrm{min}$ incubation at RT per step. The 100% ethanol was changed 3 times to assure complete removal of all water. Next, a serial drying in hexamethyldisilazane (HMDS, Sigma-Aldrich, 8.04324) was conducted using 33%, 50%, 66% and 100% HMDS, with $5\,\mathrm{min}$ for each step. The last step in 100% HMDS was conducted three times to assure removal of all ethanol. Only a thin layer of HMDS barely covering the cells was left in the specimen, and the cultures were left to dry completely out overnight at RT. A $15\,\mathrm{nm}$ thick layer of Pt/Pd was sputter coated on the samples prior to imaging (A 208 HR B Sputter Coater, Cressington). The sample was tilted from -45° to 45° with a period of $20\,\mathrm{s}$ during the sputtering.

All SEM images were acquired with an APREO Field Emission Scanning Electron Microscope from FEI using the EDT detector to record secondary electrons, with a beam current in the range of 25 – $50\,\mathrm{pA}$, and acceleration voltages between 4.0 – $10.0\,\mathrm{k}$. To avoid build-up of charges, the contact pads of the MEAs were connected to the stage using a copper tape.